Theses and Dissertations

May 2018

Hydrothermal Alteration at Devil's Kitchen in the Lassen Volcanic National Park: a Mars Analogue

Andy Wanta
University of Wisconsin-Milwaukee

HYDROTHERMAL ALTERATION AT DEVIL'S KITCHEN IN THE LASSEN VOLCANIC NATIONAL PARK: A MARS ANALOGUE

by

Andy Wanta

A Thesis Submitted in

Partial Fulfilment of the

Requirements for the Degree of

Master of Science

in Geosciences

at

University of Wisconsin Milwaukee

May 2018

ABSTRACT

HYDROTHERMAL ALTERATION AT DEVIL'S KITCHEN IN THE LASSEN VOLCANIC NATIONAL PARK: A MARS ANALOGUE

by

Andy Wanta

University of Wisconsin-Milwaukee, 2018
Under the Supervision of Dr. Lindsay McHenry

The Devil's Kitchen hydrothermal site, within the Lassen Volcanic National Park, has hydrothermal features that cover a wide range of pH conditions (2-7). Analysis of mineral precipitates, hot spring mud, unaltered substrate rock, and hot spring and meteoric water reveal a wide variety of alteration minerals, geochemical conditions, and water chemistry. Mineral suites included primary igneous phases, silica phases, clay minerals, and sulfate phases. Aluminum sulfates are the dominant sulfate species present with abundant Na^+, Fe^{3+}, and Ca^{2+} sulfate phases and less common K^+ sulfates. Amorphous silica precipitates were observed in three samples from a near-neutral hot spring and one from an acidic hot spring. When compared to the unaltered substrate, hydrothermal mud samples from acidic and near-neutral hot springs are depleted in more mobile cations (Mg, Ca, Na, and Mn) and enriched in immobile elements like TiO_2 which is consistent with acid-sulfate hydrothermal alteration with a high water-rock ratio. Altered sediments show more geochemical variation between acidic and near-neutral conditions than the mud samples. Altered sediments from acidic hot springs show variable enrichment and depletion in silica and titanium while precipitate samples from near-neutral hot springs are more enriched in aluminum and silica. Water analysis shows that high sulfate concentrations correlate with low pH waters. The hot spring waters also have a high concentration of mobile cations (Mg^+, Na^+, and Ca^{2+}) which is consistent with the waters dissolving minerals from the dacitic substrate. This wide range of hydrothermal conditions present in a small area makes Devil's Kitchen a good terrestrial analogue for the proposed

hydrothermal system at the Home Plate site on Mars. Both acid-sulfate leaching and near-neutral silica-sinter producing hot springs have been proposed to explain the deposits found near Home Plate. The Devil's Kitchen hydrothermal system could represent a terrestrial analogue where both acid-sulfate leaching and near-neutral silica-sinter deposition occur within the same system near each other.

TABLE OF CONTENTS

LIST OF FIGURES

LIST OF TABLES

ACKNOWLEDGEMENTS

Introduction

A variety of secondary minerals have been detected on Mars by orbiters and rovers including the Mars Exploration Rover (MER) Spirit, indicating widespread aqueous alteration of the ancient Martian crust. In 2004 MER Spirit landed in Gusev crater, and during its mission, it encountered some mineralogically and geochemically interesting deposits in the Columbia Hills region, specifically at Home Plate. Spirit observed silica-rich soils, sulfate-rich soils, and silica-rich nodules near the Home Plate site. The data collected suggests an ancient hydrothermal system that altered the basaltic substrate (Schmidt et al., 2008). However, the chemical conditions associated with the hydrothermal fluids that formed the silica-rich soils and the silica-rich nodules are still a matter of debate. Researchers now focus on two competing models to explain these deposits; either acid-sulfate leaching (e.g. Squyres et al., 2008) or precipitation by a near-neutral hot spring (e.g. Ruff et al., 2011). These are important models to study because near-neutral hot springs are much more likely to harbor life, and a greater diversity of life, than acid-sulfate hot springs or fumaroles (e.g. Goorissen et al., 2003; Krebs et al., 2014). On Earth, hot spring environments are teeming with microbial life, while acid sulfate fumaroles have much lower abundances and diversity of extremophile organisms (Goorissen et al., 2003; Krebs et al., 2014). Hydrothermal sites provide a localized source of heat, water, and elements (e.g. sulfur, phosphorous, and oxygen) needed for chemosynthesis (Yen et al., 2008). Hydrothermal sites could have persisted long after the rest of the Martian surface had cooled and desiccated, creating localized oases that could have sustained conditions suitable for life. To determine the composition and chemical characteristics of the hydrothermal fluid and the environmental conditions associated with these features, we need to study Earth analogues.

This study aims to add to our understanding of the habitability of hydrothermal environments on Earth and how they relate to Martian hydrothermal environments. This was accomplished by characterizing the mineralogy and water chemistry associated with the hydrothermal system at Lassen Volcanic National Park in Northern California. Lassen's hydrothermal system is a good analogue for the inferred Columbia Hills hydrothermal system because it contains a variety of hydrothermal features covering a wide spectrum of pH, oxidation/reduction potential, and water chemistry in a relatively small area, as determined during this study. The pH of the hot springs is controlled by the sulfate content of the water, which our results show to range from <10 ppm in the neutral (pH of 7.4) hot springs to 150 ppm in the most acidic (pH of 2.0) hot spring. Redox conditions also vary greatly from site to site, with oxidation/reduction potential (ORP) values of 590 mV in the most acidic hot spring and 120 mV in the neutral hot spring. These hot springs have a relatively consistent temperature, ranging from 66° to 92°C while the nearby stream was measured at 9.3° to 15°C.

These diverse conditions yield a wide variety of mineral assemblages including primary igneous phases, silica phases, multiple sulfates and clay minerals. SEM analysis revealed abundant biological structures incorporated into the mineral samples analyzed. These biological structures demonstrate both the habitability of these environments and the preservation potential of biosignatures in hydrothermal environments. This diverse suite of alteration minerals and water chemistry makes the Lassen hydrothermal system a good terrestrial analogue for the inferred hydrothermal deposit observed by the MER Spirit near Home Plate in the Columbia Hills on Mars. We can compare the alteration products at Lassen to the preserved products on Mars to determine whether the same conditions were likely present on early Mars.

Characterizing the mineralogical patterns and water chemistry associated with each of these hydrothermal features allows us to determine what factors control the astrobiologically-relevant environmental conditions (pH, temperature, oxidation/reduction potential, and chemical composition).

Objectives

The main objectives of this study are to: 1) Characterize the mineralogical and geochemical patterns associated with different hydrothermal features in the Lassen hydrothermal system; 2) Constrain the environmental factors that control their alteration mineralogy; 3) demonstrate the habitability of the environment and the preservation potential of biosignatures; and 4) Compare the geochemical and mineralogical patterns found at Lassen to the ones observed by the MER Spirit near Home Plate.

To achieve these objectives I analyzed the mineralogical and geochemical patterns of mineral and water samples from the Devil's Kitchen hydrothermal site. I acquired mineralogical data using X-Ray Diffraction (XRD), geochemical data for precipitate and mud samples using X-Ray Fluorescence (XRF), and some mineralogical data using a Scanning Electron Microscope (SEM) with an Energy Dispersive X-Ray Spectroscopy (EDS) system. SEM was also used to find and image biological structures present in the samples, which helped demonstrate the habitability of the environment and the likelihood of biosignature preservation. I also analyzed the chemistry of hot spring and meteoric water samples using an Ion Chromatograph and Atomic Adsorption to determine the dissolved anions and cations respectively.

Background

Terrestrial Hydrothermal Environments

Hydrothermal environments produce a wide variety of alteration mineral assemblages and geochemical trends. The alteration mineral assemblage and geochemical trends formed in a hydrothermal environment depend on a variety of factors including water-rock ratio, pH and geochemical conditions of the water, and substrate composition. Understanding how these factors control alteration mineral assemblages is important when making comparisons to Martian analogues.

Hydrothermal alteration is caused by volatile-rich steam and water interacting with the bedrock. These volatile-rich fluids are produced upon depressurization boiling of deep meteoric fluids that produce steam rich in volatiles like CO_2, H_2S, and H_2 while a neutral to alkaline liquid phase, rich in non-volatiles, is separated from the steam (e.g. Markusson and Stefansson, 2011). Following fluid segregation, the volatile rich steam mixes with oxygenated surface waters and atmospheric oxygen and produces acid sulfate waters that readily dissolve bedrock and form alteration products (Arnorsson et al., 2007). These alteration mineral assemblages include sulfates, sulfides, clay minerals, silica phases, and residual primary igneous minerals depending on substrate composition, water-gas-rock interaction, and fluid chemistry (e.g. Lynne et al., 2007; Markusson and Stefansson, 2011; Hynek et al., 2013; McHenry et al., 2017). Alteration mineral assemblages in gas-dominated systems with a low water-rock ratio can come from either direct precipitation from the vapor phase or leaching of the wall rock (Hynek et al., 2013). The alteration mineralogy depends on the substrate and the steam compositions. During their study on Nicaraguan volcanoes, Hynek et al. (2013) observed that the mineral

4

assemblages surrounding particular fumaroles depended on the pH of the vapor. They observed mineral assemblages at fumaroles with low pH (-1 to 1) dominated by gypsum, native sulfur, and amorphous silica while at higher pH (6) calcite was more dominant. When analyzing the fluid chemistry of the fumaroles and hot springs in Nicaragua, Hynek et al. (2013) observed that the major control on ion concentration is pH. More acidic fluids were associated with higher concentrations of dissolved ions while changes in temperature had little to no affect.

In Iceland, at the Krýsuvik geothermal area, Markusson and Stefansson (2011) observed that the alteration mineral assemblages appeared to be related to the proximity and intensity of surface activity and the mixing ratio of geothermal steam and cold meteoric water. The areas nearest to the steam vents with the highest supply of H_2S have mineral assemblages that reflect less oxidation while more distal areas showed more oxidized mineral assemblages. Siliceous phases can be found in hydrothermal environments and can take a variety of forms including Opal-A, Opal-CT, Opal-C, amorphous silica, and quartz phases. Silica sinters form where nearly neutral pH, alkali chloride waters discharge at the surface (Lynne et al., 2006). Silica sinters are important for habitability studies because they can preserve biosignatures of past environments because the rapidly precipitating silica coats all surfaces, including microbes thriving in the thermal waters (Cady and Farmer, 1996).

Lassen

Lassen Volcanic National Park lies at the southern end of the Cascade Range in Northern California. The Lassen system is mostly andesitic to dacitic in composition. While this is different from the high-Fe-basaltic composition that is most widespread on Mars, the alteration patterns of the two compositions can be similar (e.g. McHenry et al., 2013). The Lassen area is home to

the largest active hydrothermal system in the Cascades Range with a variety of hydrothermal features including fumaroles, hot springs, and mud pots (Janik and McLaren, 2010; Ingebritsen et. al., 2016). The hydrothermal system is roughly 315,000 years old and formed due to the onset of silicic volcanism (Crowley et al., 2004). Lassen Peak is the currently active volcanic center in the park, and last erupted as in 1915. Volcanism in the Lassen Volcanic Center started about 825,000 years ago with the formation of the Rockland Caldera Complex followed by the formation of Brokeoff Volcano 550,000 years ago (Janik and McLaren 2010). These earlier volcanic episodes have associated ancient hydrothermal systems (John et al., 2005). Water-rock interaction in the hydrothermal areas alters the volcanic rock into easily erodible clays and other alteration products. As a result, the distribution of the acid-sulfate discharge tends to be highly transient in space and time (Ingebritsen et al., 2016). The Devil's Kitchen site, the focus of this research, is located southwest of the main hydrothermal area (Figure 1) along a mapped fault system (Janik and McLaren 2010). Deglaciation and the large dacitic eruptions at 27 and 1.1 ka are likely to have affected the hydrothermal system. In fact, sinter deposits several meters thick occur at two sites in the Devil's Kitchen area, indicating that high-chloride waters discharged there in the past (Muffler et al., 1982). Devil's Kitchen is monitored by the USGS hydrothermal monitoring network in the Cascade Range so hourly measurements of heat discharge and acid-sulfate discharge were collected between 2009 and 2016. This high-frequency data revealed a dynamic system which shows seasonality, responses to short-term weather events, and sensitivity to small- to moderate scale seismicity (Ingebritsen et al., 2016).
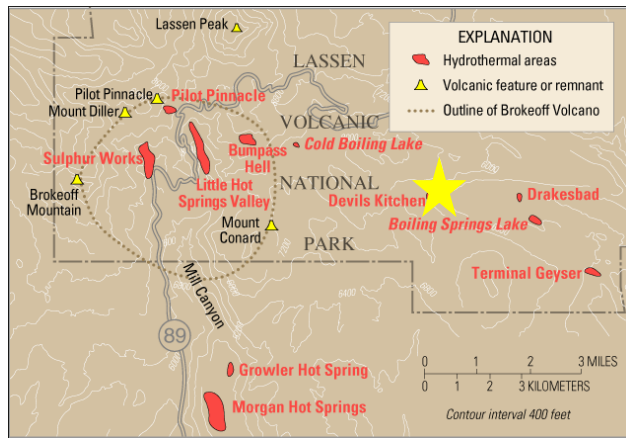
Figure 1: Map of the southwestern quarter of Lassen Volcanic National Park. The dot-dash line shows the park boundary. The hydrothermal features in the park are red on the map. Devil's Kitchen (yellow star) is southeast of Lassen Peak beyond the boundaries of the former Brokeoff Volcano (USGS Factsheet, Clynne et al., 2003).

In the current Lassen hydrothermal system, meteoric water percolates down and is heated by molten rock at depth (Figure 2). As the now hot water rises, the confining pressure on it is released and it boils, resulting in a "two-phase" hydrothermal system. The volatile (and acidic) compounds preferentially go into the steam phase, leaving a depleted, more neutral chlorine-rich liquid phase behind (e.g. Clynne et al., 2003). The volatile-rich steam phase rises through the subsurface and drives the acid-sulfate fumaroles, mudpots, and hot springs. The pH of these features ranges from about 2 to 7, with temperatures between 80-100°C as measured during this current study. Devil's Kitchen lies within this acid-sulfate steam driven region.
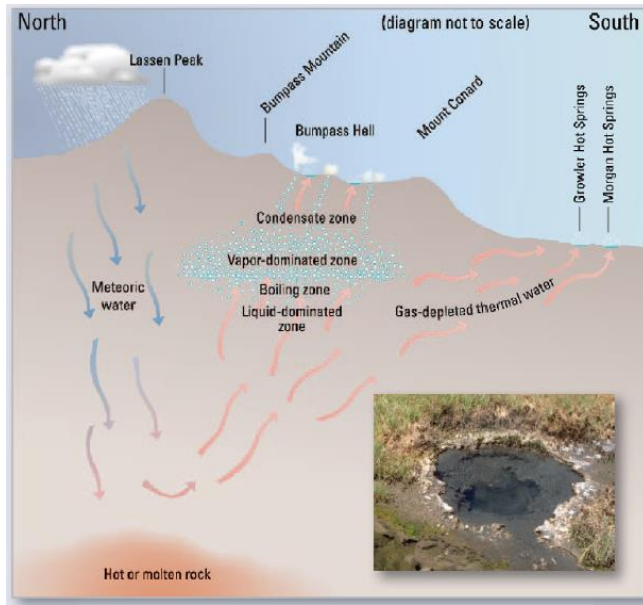
Figure 2: Diagram showing the "two-phase" hydrothermal system at Lassen. Meteoric water percolates down to the hot rocks at depth. Then they rise and undergo phase separation with the volatile phases going into the steam phase and a gas depleted, chloride-rich water running off to lower elevations (Clynne et al., 2003).

The Devil's Kitchen hydrothermal area is in the south central portion of the park and lies outside of the boundaries of the former Brokeoff Volcano. The hydrothermal site consists of multiple hydrothermal features on a relatively flat platform at the base of a steep talus slope and cliff feature about 100 meters high. A small stream called Hot Springs Creek defines the northern border of the hydrothermal area and flows west to east along the hydrothermal site. The main hydrothermal area consists of about a dozen different hot springs and fumaroles ranging in size from half a meter to 3 meters across and covering an area about 100 meters across. This hydrothermal field yields a total steam upflow of 8 kg/s (Ingebritsen et al., 2016). Devil's Kitchen is a good analogue for the inferred hydrothermal area at Columbia Hills because it encompasses both acid-sulfate leaching and precipitation from near-neutral hydrothermal waters. The wide range of pH (2-7) present on a local level allows us to study potential

differences between the mineralogical and geochemical patterns associated with different pH hydrothermal features.

Mars

The Martian crust differs from Earth's crust, being largely comprised of high-Fe-basalts (McSween et. al., 2009). During its mission to Gusev crater the Mars Exploration Rover (MER) Spirit analyzed late Noachian aged outcrops and soils at the Columbia Hills site (Arvidson et al., 2008). At the Home Plate feature within the Columbia Hills basin, Spirit encountered a small platform of layered clastic rocks of Barnhill class (Squyres et al., 2004), interpreted as laminated and cross bedded tephra. The tephra showed a bomb sag structure (Figure 3), which suggest that there was explosive volcanism nearby (Schmidt et al., 2008). The morphology of the bomb sag structures also suggests that the substrate was wet at the time of the bomb impact (Squyres et al., 2007). This would be consistent with a hydrothermal site near the flanks of a volcano. Hydrothermal activity was likely common on Mars due to evidence of early aqueous activity and extensive volcanism (e.g. Hynek et al., 2010).

Figure 3: False color image of the bomb sag structures in the tephra layers near Home Plate. The bomb sag morphology suggests that the material the bomb impacted was wet. Figure from Squyres et al. (2007).

During its mission to Home Plate, Spirit accidentally disturbed the soil with its broken wheel and excavated a series of trenches adjacent to Home Plate (Figure 4), exposing discrete packets of soil that were sulfate-rich, and exposed other geographically separate soils that were rich in silica and titanium (Ruff et al., 2011). The sulfate-rich sediments were white to yellow soils in the Paso Robles class and composed of hydrated sulfate salts that were likely fumarolic in origin (Yen et al., 2008). The Paso Robles class sulfate soils contained up to 35 wt% sulfate (Schmidt et al., 2008). Sediments containing elevated silica and Ti contents support the idea of a hydrothermal origin but don't unambiguously indicate either a neutral or acidic environment (Squyres et al., 2008).
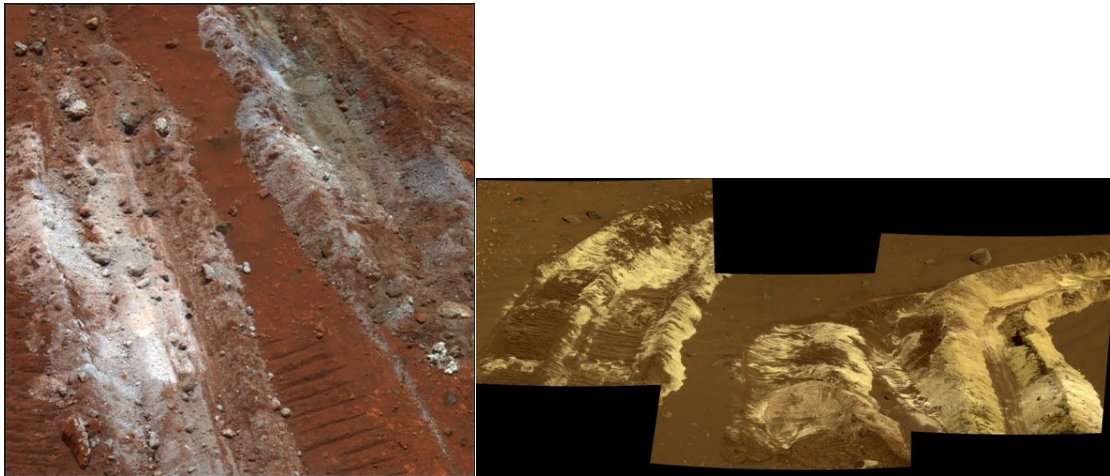
Figure 4: Left: trench near Home Plate that Spirit accidentally excavated with its broken wheel, revealing a deposit called Kenosha Comets of almost pure silica. Right: similar trench composed predominantly of sulfate minerals. The sulfur-rich soils were informally named Tyrone. (Nasa Jet Propulsion Laboratory website)
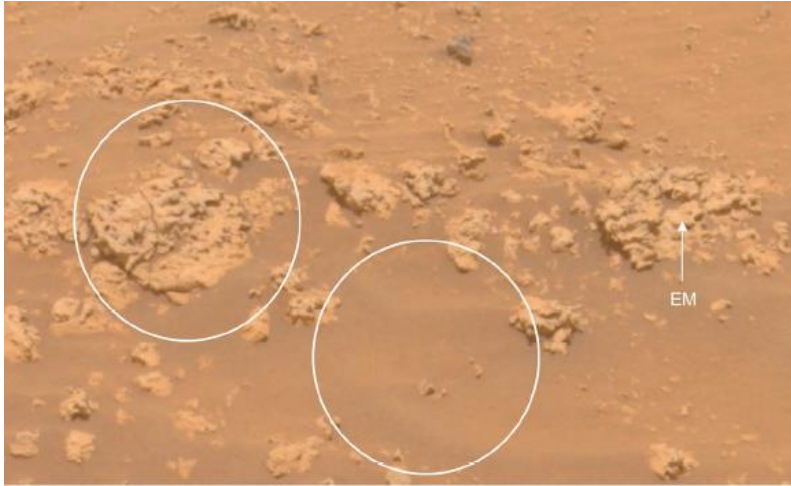
Figure 5: Pancam approximate true color image of a silica-rich nodular outcrop (circled). EM is the Elizabeth Mahon target silica-rich nodule (Adapted from Ruff et al., 2011).

Spirit observed silica-rich materials concentrated in the Eastern Valley but also found them elsewhere in the Home Plate region (Schmidt et al., 2008). Spirit also observed a number of silica-rich nodular outcrops adjacent to the Home Plate raised platform (Figure 5). Locations of these outcrops can be seen in Figure 6. The observed enrichment of silica in the soil found in close association with volcanic materials and, in some cases, intimately mixed with ferric sulfates that are probably of hydrothermal origin, suggest a hydrothermal origin for these sediments (Yen et al., 2008). The silica phase present in the soils is opal-A, which is compelling evidence for a hydrothermal system (Squyres et al., 2008). The controversy is whether the enrichment in silica was produced by leaching of other, more mobile constituents of basalt by acidic condensates of fumaroles (e.g. Squyres et al., 2008), or by direct precipitation as silica sinter in a neutral hot spring environment (e.g. Ruff et al., 2011). Understanding whether these proposed hydrothermal deposits are the product of an acidic hydrothermal environment or a near-neutral one has important implications for potential habitability. In either case, the

11

presence of hydrothermal sites on the Martian surface is extremely important because they

could have provided the necessary materials and energy sources for life (Martin et al., 2008).
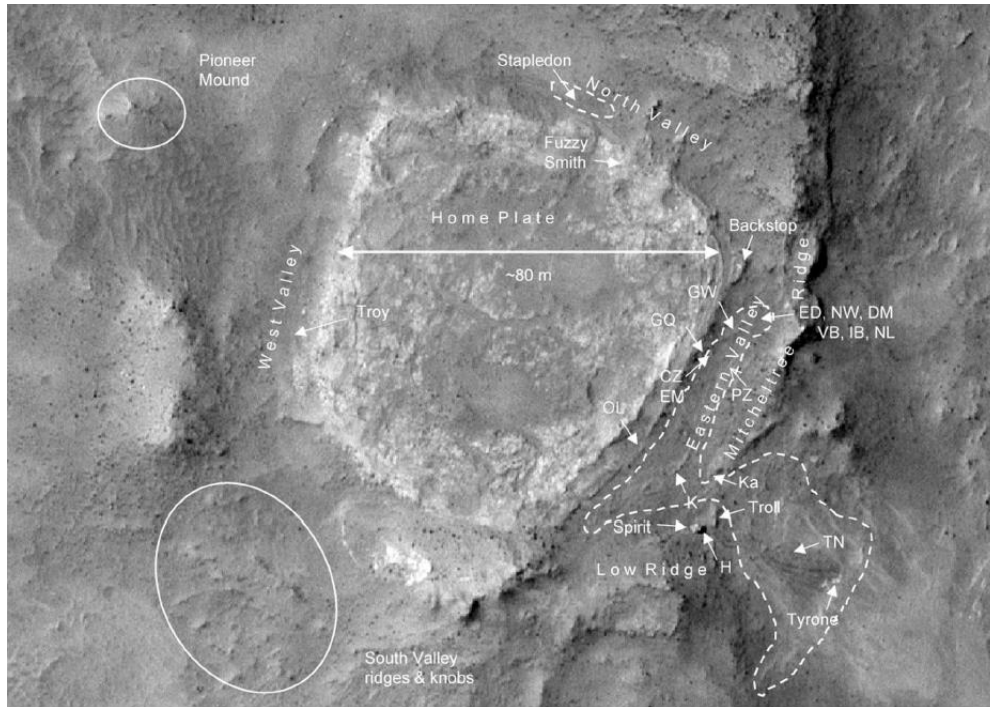
Figure 6: A portion of HiRISE image PSP_001515_1655_RED showing Home Plate and vicinity with Spirit parked at Low Ridge. Examples of silica-rich nodular outcrops include Tyrone Nodules (TN), Innocent Bystander (IB), Norma Luker (NL), and others. Gertrude Weise (GW) is the silica-rich soil. Halley (H) is the sulfur-rich outcrop. Dashed lines indicate approximate extent of recognized and likely silica-rich nodular outcrops (Adapted from Ruff et al., 2011).

Any process that involves precipitation of silica from fluids can also provide a

mechanism for preserving evidence of microbes (Cady and Farmer 1996), but near-neutral

hydrothermal environments are more habitable than acid-sulfate environments. On Earth, life

can still exist in acidic environments, but the biomass and diversity are much lower than in

near-neutral environments (Goorissen et al., 2003). Near-neutral silica sinters can also readily

encrust any biological structures and preserve biologically mediated textures, preserving

biosignatures (e.g. Ruff and Farmer 2016).

Ruff and Farmer (2016) suggest that the silica nodules found adjacent to Home Plate are evidence of precipitation from near-neutral hot springs. The nodules were discovered using the Mini-TES (Miniature Thermal Emission Spectra) near the Tyrone light-toned soil deposit. The nodules and the Tyrone light-toned soil deposit exhibited the spectral signature associated with high silica contents. The spectral signature was consistent with opaline silica, which is distinct from quartz or cristobalite (Michalski et al., 2008). The opaline silica nodules found at Home Plate were remarkably similar to silica nodules found in neutral hydrothermal discharge from hot springs at El Tatio in Chile (Figure 7) (Ruff and Farmer 2016). The silica nodules at El Tatio are biologically mediated deposits that preserve biological structures and evidence of life; if the silica deposits near Home Plate were formed by the same process, they would be a biosignature and evidence for past life on Mars. Further textural and chemical analyses would be required to determine if the opaline silica nodules near Home Plate are biologically mediated or not, but they are still evidence for a near-neutral hydrothermal system (Ruff and Farmer 2016).
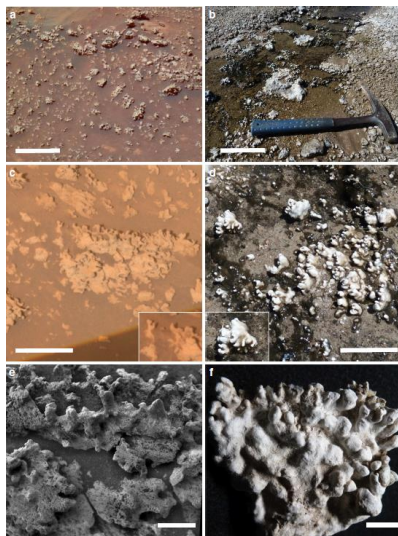
Figure 7: Side-by-side comparison between the digitate silica nodules observed by Ruff and Farmer (2016) at El Tatio Geyser in Chile (right panel) and the silica-rich nodular outcrops found adjacent to Home Plate by Spirit (left panel).

It is important to understand the environmental conditions represented by the soils and outcrops found around the Home Plate area. We need to be able to determine if this inferred, ancient hydrothermal site was created by acid-sulfate alteration, near neutral hot springs, or some combination of both. Determining the environmental conditions and possible habitability of these ancient hydrothermal features is important for understanding their astrobiological potential (Hynek et al., 2013). To understand the environmental conditions that control the alteration patterns of hydrothermal systems, we need to study Earth analogues. We need to characterize hydrothermal alteration mineralogy and its relationship to habitability so that we can compare terrestrial hydrothermal systems to the ancient hydrothermal systems found on Mars.

Field Methods

Field samples were collected in October of 2016 and August of 2017. To collect mineral and water samples from a broad and representative suite of hydrothermal conditions, I prospected the hydrothermal field with pH papers and a thermometer. Once a representative suite of hot springs was chosen, water samples were filtered with 0.2 micron sterile syringe filters and collected for further analysis in the lab. Temperature and pH measurements were collected in situ and recorded. Water samples were also collected and analyzed in the field using the Hydrolab Sonde (Figure 8), which measures total dissolved solids, salinity, pH, conductivity, and oxidation/reduction potential.

Figure 8: Undergraduate assistant Ashley Stewart analyzing a water sample with the Hydrolab Sonde.

All water samples collected were analyzed in the field for iron and bicarbonate concentrations. The iron concentration was analyzed using CHEMets self-filling ampoules for colorimetric analysis (Iron R-6001). The bicarbonate concentration was calculated using a nitric acid titration where pH was measured using a Fisher Scientific accumet hand-held pH probe. Mineral, sediment, and rock samples were then collected near each hot spring. We strived to sample each distinct mineral assemblage associated with each hot spring by collecting a sample of each different colored mineral deposit and crystal habit (Figure 9-15). Each sample was described, bagged, and labeled. A mud sample was collected from underneath the water line in each hot spring sampled. Photographs with scales were taken at each sampling location to document the position of samples relative to the associated hot spring. During the 2017 field season I sampled two silica coatings (samples L-17-DK-04 and L-17-DK-27). L-17-DK-04 was sampled from the waterline of the pH 5 hot spring in site #1. Silica crust sample L-17-DK-27 was collected from the waterline of the pH 3.2 hot spring at site #5. Descriptions of all samples collected in the field in 2016 and 2017 are shown in Tables 1 and 2.

2016 Samples	Sample Type	Description	Temp (°C)	pH
L-16-DK-01	water	upstream water sample	9.3	5
L-17-DK-02	water	small hot spring	90.9	3.5
L-16-DK-03	mud	gray mud collected below water line	90.9	
L-16-DK-04	precipitate	encrusting white mineral	92	
L-16-DK-05	water	clear boiling hot spring	92	5
L-16-DK-06	sediment	white encrusting mineral	62.6	
L-16-DK-07	sediment	hard encrusting white mineral	92.7	
L-16-DK-08	water	acidic hot spring	80.4	2
L-16-DK-09	mud	gray mud collected below water line	70.6	
L-16-DK-11	precipitate	crystalline white mineral	65	
L-16-DK-12	sediment	altered rock with white coating	61.6	
L-16-DK-13	precipitate	orange precipitate	61.6	
L-16-DK-14	sediment	yellow and green coated altered rock	62	
L-16-DK-15	water	neutral hot spring	8.4	7.4
L-16-DK-16	precipitate	dark gray foam	86.2	
L-16-DK-17	mud	gray mud collected below water line	84.4	
L-16-DK-18	sediment	green coating on rock	61.7	
L-16-DK-19	sediment	beige to gray chunky mineral	50.5	
L-16-DK-20	sediment	thin white crust on altered rock	50.5	
L-16-DK-21	sediment	red coating on rock	67	
L-16-DK-22	water	downstream water sample	15.4	7.2

Table 1: Descriptions of all mineral and water samples collected in 2016 with associated sample type, temperature, and pH. Boxes denote minerals and water samples collected from the same hot spring feature.

2017 Samples	Site Number	Sample Type	Description	Temp (°C)	pH
L-17-DK-01	1	water	mildly bubbling hot spring	88.1	6.12
L-17-DK-02		sediment	grey mud; sampled below water line	71	
L-17-DK-03		sediment	green/orange algae/clay mix; crust on margin of hot spring	55	
L-17-DK-04		sediment	white/beige surface coating	60	
L-17-DK-05		precipitate	yellow/white precipitate sampled from above hot spring	47.4	
L-17-DK-06	2	water	mildly bubbling hot spring	83.8	2.65
L-17-DK-07		sediment	side wall mud	34.3	
L-17-DK-08		sediment	grey mud; sampled below water line	83.8	
L-17-DK-09		precipitate	mixed bag of precipitates	43.2	
L-17-DK-10		precipitate	mixed bag of precipitates	43.2	
L-17-DK-11		precipitate	mixed bag of precipitates	43.2	
L-17-DK-12	3	water	vigorously boiling hot spring	88.9	2.74
L-17-DK-13		sediment	grey mud; sampled below water line	88.9	
L-17-DK-14	4	sediment	dark black/grey clay coating	85.2	
L-17-DK-15		precipitate	white crusty ppt on margin of spring	67.2	
L-17-DK-16		sediment	grey mud; sampled below water line	81.4	
L-17-DK-17		precipitate	soft precipitate adj. to hot spring	67.2	
L-17-DK-18		sediment	nodular silica + clay	29.4	
L-17-DK-22		water	neutral spring; vigorous boil + steam	83	6.73
L-17-DK-23	5	water	small hot spring	85	3.19
L-17-DK-24		sediment	grey mud; sampled below water line	65	
L-17-DK-25		sediment	dug from ~10cm beneath wall surface	49.3	
L-17-DK-26		sediment	hard red mud w/ deep orange crust	71.5	
L-17-DK-27		sediment	Banded crust at water margin	62.7	
L-17-DK-28		precipitate	white/yellow ppt on surface	48.6	
L-17-DK-29	Downstream	water	downstream water sample	16.4	6.68
L-17-DK-30	Upstream	water	upstream water sample	10.9	7.12
L-17-DK-31	GPS Point 340	precipitate	orange 'cauliflower' precipitate	46.3	
L-17-DK-32		precipitate	white/yellow precipitate	51.8	
L-17-DK-33	6	water	hot spring water	85.8	3.02
L-17-DK-34		precipitate	yellow ppt just below water level	51.3	
L-17-DK-35		sediment	grey mud; sampled below water line	82.4	
L-17-DK-36		precipitate	orange ppt above yellow ppt (DK-34)	53.3	

Table 2: Descriptions of all mineral and water samples collected in 2017 with associated site number, sample type, temperature and pH. Boxes denote minerals and water samples collected from the same hot spring feature.

Figure 9: Site 1: Samples collected in 2016 include L-16-DK-06 and L-16-07; samples collected in 2017 include L-17-DK-02 to L-17-DK-05. Jacob's staff is shown for scale.
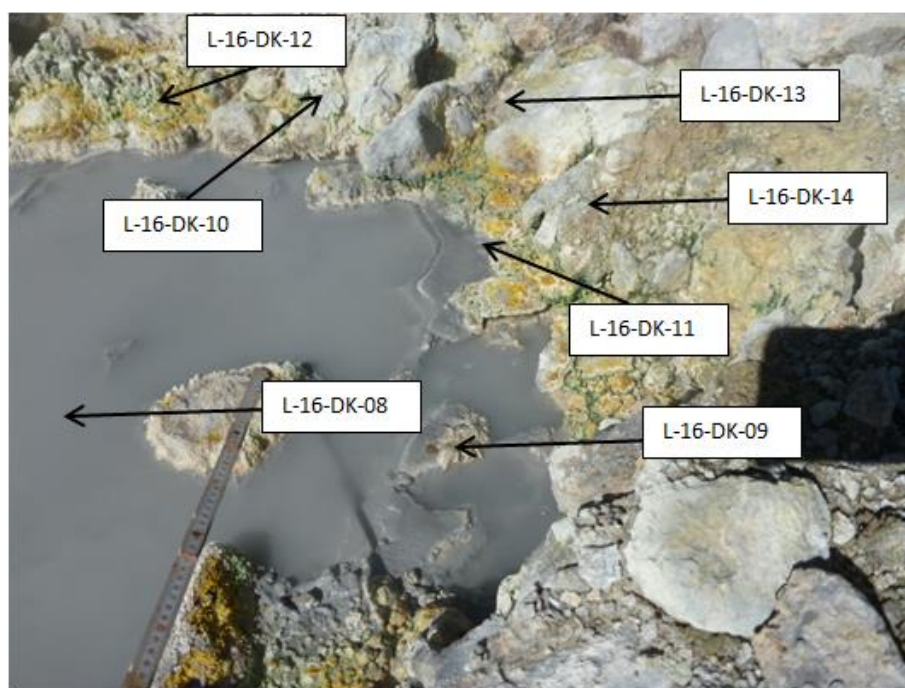
Figure 10: Site 2: In 2016, samples L-16-DK-08 to L-16-DK-14 were collected from around this hot spring and in 2017 samples L-17-DK-07 to L-17-DK-11 were collected. A foldable meter stick is shown for scale

Figure 11: Site 3: Sampled only in 2017: L-17-DK-12 and L-17-DK-13

Figure 12: Site 4: Samples collected in 2016 include L-16-DK-15 to L-16-DK-20; samples collected in 2017 include L-17-DK-14 to L-17-DK-18 and water sample L-17-DK-22.

19
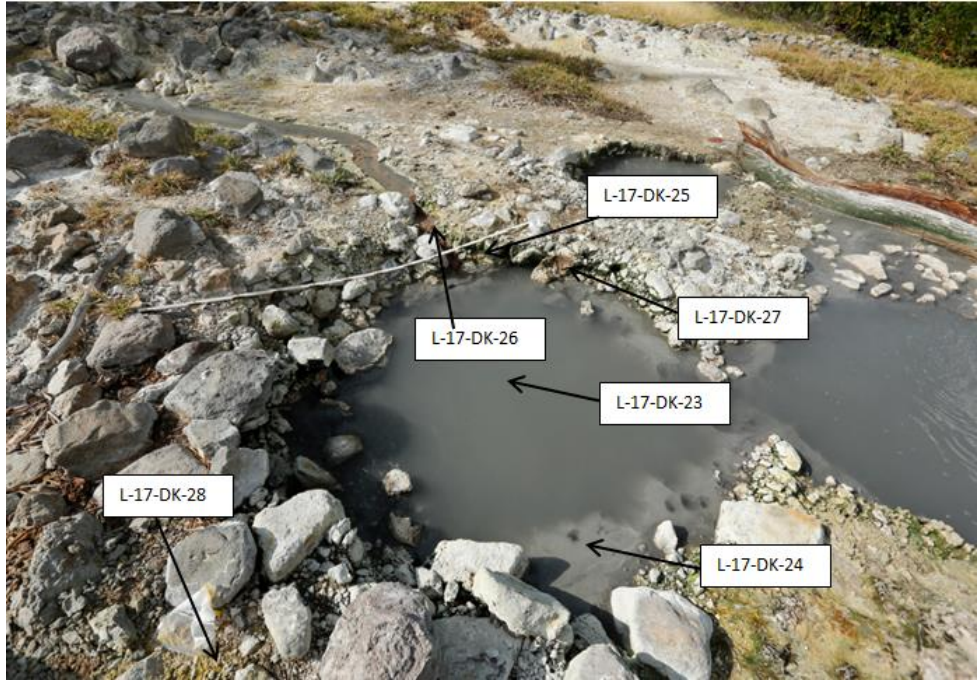
Figure 13: Site 5: Samples collected from this hot spring in 2017 only and include: L-17-DK-23 to L-17-DK-28. Foldable 2-meter stick is shown for scale.

Figure 14: Site 6: Samples collected from this hot spring in 2017 only. Samples include: L-17-DK-33 to L-17-DK-36.

Figure 15: Discharge stream where L-16-DK-21 was sampled in 2016. Jacob's staff is shown for scale.

I used Google Maps and the GPS coordinates for each sample site to generate a map showing the six main sample locations from the 2017 field season (Figure 16). A piece of unaltered substrate was sampled from a site well above the hydrothermal area to determine the original rock composition. In addition to collecting water samples from the hot springs themselves, we collected samples of meteoric water from the stream that runs around the hydrothermal site. One sample was collected from upstream of the hydrothermal area to get an "uncontaminated sample" and one sample was collected from downstream to see how the hydrothermal site altered the chemistry of the stream.

Figure 16: Map (base map from Google Earth) showing the six different sample sites in the Devil's Kitchen area and the location of the upstream and downstream water samples. Scale bar in the bottom right corner is 50 m.

Lab Methods

X-Ray Diffraction

Samples were air dried in aluminum trays for several days. Dry samples were powdered by hand using a mortar and pestle, to avoid potential heating or dissolution. The powders were mounted in a cavity mount with a gently smoothed surface and analyzed using a Bruker D8 Focus X-Ray Diffractometer (XRD) using Cu Kα radiation, 1s per 0.02° 2θ, 2°-60° range, and scintillation detector following the methods of McHenry et al., 2017. The XRD patterns were analyzed using Bruker's EVA software (comparing against the Centre for Diffraction Data (ICDD) PDF-2 database) to identify the mineral phases present and their relative abundances.

X-Ray Fluorescence

The XRF preparations use the same air-dried samples as the XRD, but the powders were ground using a shatterbox. Powders were heated in a 105°C oven for approximately 12 hours to drive off any residual water. A split of each sample was carefully weighed (+/- .0003g) and then heated in a ceramic crucible in a 1050°C muffle furnace to drive off any volatile constituents. The percent loss on ignition (%LOI) was calculated for each sample. Next, a separate split of each sample was fused into a glass bead, by combining 1 +/- .0003 grams of sample with 10 +/- 0.0003g of a 50:50 lithium metaborate/tetraborate flux (with integrated LiBr non-wetting agent) and 1 +/- 0.0003g of ammonium nitrate (oxidizer). The combined powders were thoroughly mixed and then fused for approximately 20 minutes using a Claisse M4 fluxer. The glass beads were analyzed using a Bruker S4 Pioneer Wavelength Dispersive XRF; results were calibrated using a calibration curve derived from 11 USGS rock standards (detailed methods of McHenry, 2009; Byers et al., 2016). Major element analyses with analytical errors above 2% (12% for trace elements), or concentrations less than twice the lower limit of detection (LLD), were reported as not detected. Spider plots were prepared using Microsoft Excel by normalizing the elemental concentrations to the unaltered substrate composition and plotting the amount of variation in each element on a log scale.

Samples that had %LOI values above 50% could not be fused into beads, and were thus prepared and analyzed as pressed pellets where sufficient material was available. For these samples, 7.5 grams of dried and powdered sample was combined with three Bruker GeoQuant wax binder pellets (0.94 grams total) using a shatterbox for 30 seconds. Where less than 7.5 grams of sample was available, 5.0 grams of dried and powdered sample was combined with

two Bruker GeoQuant wax binder pellets using the shatterbox. The powder was then pressed in a 40mm die using an Atlas T25 press at 25 tons for 1 minute (McHenry et al., 2017). The pressed pellets were analyzed using a Bruker S4 Pioneer Wavelength Dispersive XRF; results were calibrated using a calibration curve derived from six USGS rock standards (detailed methods of McHenry, 2009; Byers et al., 2016). The samples prepared as pressed pellets had sulfur concentrations well above the calibrated range and could thus not be calculated.

Scanning Electron Microscope

Two silica coating samples were collected in 2017 (L-17-DK-04 and L-17-DK-27) and analyzed using Scanning Electron Microscopy (SEM). These samples were air dried in an aluminum tray and then cut into pieces (labeled L-17-DK-04A, L-17-DK-04B etc.) using a combination of a wet saw and a fine-toothed wire saw. When cutting the sample, care was taken to preserve its original exterior textures. Individual pieces were glued to stubs using carbon glue. L-17-DK-04A, B, and C and L-17-DK-27A and B were coated with approximately 8-12 nanometers of iridium using an Emitech K575X Sputter Coater. L-17-DK-04D, E and F were carbon coated in an Edwards Vacuum Coating unit. When the samples were not being analyzed, they were kept in a vacuum chamber to reduce the effect of outgassing during image capturing. The samples were analyzed using a Hitachi S-4800 Field Emission Scanning Electron Microscope (FE-SEM) equipped with a Bruker Quantax energy-dispersive spectroscopy (EDS) system. Secondary electron imaging provided textural information and identification of biological structures present in the sample while the EDS provided qualitative elemental abundances which aided mineral identification.

Water

The water samples were analyzed using an Ion Chromatograph (IC) to measure anion concentrations and an Atomic Absorption Spectrometer (AA) to measure cation concentrations, using the ASTM Standard Methods for Examination of Water and Wastewater, 17th ed (1989) for AA analysis and the methods of the ASTM Standard Methods for Examination of Water and Wastewater, 17th ed. (1989) and the methods for Ion Chromatography of James Fritz et al., (1989). The samples were filtered using 0.2 micron sterile syringe filter to remove any suspended particles. For the IC analysis, the water samples were put into a 15 mL polystyrene screw top test tube and then mounted into the instrument and run over night. For AA analysis, the water samples were diluted 1:10, 1:50, or 1:100 depending on the concentration of the dissolved ions. For sulfate and phosphate the samples were not diluted. Calibration curves were made by analyzing standards of known concentrations. Samples were plotted on these curves to calculate concentration in parts per million (ppm).

Results

XRD

The mineral phases observed vary widely between different hot springs. The main categories into which the mineral suites fall are primary igneous phases, clay minerals, and sulfates. Primary mineral phases were present in all samples analyzed and reflect the original plagioclase-rich dacitic to andesitic substrate. The dominant silica phase present was tridymite. Native sulfur or a wide range of sulfate minerals are abundant throughout the hydrothermal system. Aluminum sulfates are the dominant sulfate phases present and are associated with features across the entire range of pH. The other sulfate species present include Ca^{2+}, K^+, Fe^{3+},

Na$^+$, and Mg^{2+} with most species occurring near both high and low pH hot springs. Kaolinite was

the dominant clay mineral phase, with montmorillonite present in only three samples (Table 3).

Individual hydrothermal sites sampled in both 2016 and 2017 showed variation in the

precipitates present. Hydrated aluminum sulfates including alunogen (Al$_2$(SO$_4$)$_3\cdot$ 17H$_2$O),

tamarugite (NaAl(SO$_4$)$_2\cdot$6H$_2$O) , and halotrichite (FeAl$_2$(SO$_4$)$_4\cdot$ 22H$_2$O) were the most common

precipitates found in 2017 and were observed at all sites. Smaller amounts of other sulfates

were also present. Representative XRD patterns are shown in the appendix (Figure 34-41).

Table 3 — Mineral phases present in each sample and their relative abundances.

Sample #	SiO2 minerals				Igneous Minerals		Clay Minerals				Sulfates									Other			pH of hot spring	
	Tridymite	Cristobalite	Quartz	Amorphous Silica	Plagioclase	Potassium Feldspar	Kaolinite	Montmorillonite	Dickite	Illite	Gypsum $CaSO_4 \cdot 2H_2O$	Tamagurite $NaAl(SO_4)_2 \cdot 6H_2O$	Alunogen $Al_2(SO_4)_3 \cdot 17H_2O$	Quenstedtite $Fe_2(SO_4)_3 \cdot 11H_2O$	Alunite $KAl_3(SO_4)_2(OH)_6$	Halotrichite $FeAl_2(SO_4)_4 \cdot 22H_2O$	Hexahydrite $MgSO_4 \bullet 6(H_2O)$	Jarosite $KFe^{3+}_3(OH)_6(SO_4)_2$	Aluminocopiaptite $Al_{2/3}Fe^{3+}_4(SO_4)$	Sulfur	Pyrite	No Diffraction	pH of hot spring	
L-16-DK-03	XXX				XX															XX			3.2	2016 SITE ONLY
L-16-DK-04												XXX	XX			XX							3.2	
L-17-DK-02					XXX	XX	XXX		XX														6.1	SITE 1 2017
L-17-DK-03																						XXX	6.1	
L-17-DK-04 BULK	XXX	XX		XX	XX																		6.1	
L-17-DK-04 COATING	XXX	XXX		XXX	XX						XX				X						X		6.1	
L-17-DK-05	XXX	XX			XXX							XXX	XXX			XXX							6.1	
L-16-DK-06	XXX				XX																		5.4	SITE 1 2016
L-16-DK-07			XX		XX																		5.4	
L-16-DK-09	XXX				XX															XX			2.2	SITE 2 2016
L-16-DK-11	XX				XX							XX						XX					2.2	
L-16-DK-12	XXX				XX		XX		XX														2.2	
L-16-DK-13								XX	XX														2.2	
L-16-DK-14	XXX				XX																		2.2	
L-17-DK-07	XXX					XX			XX									X					2.6	SITE 2 2017
L-17-DK-08	XXX				XXX	XX	XXX													XX			2.6	
L-17-DK-09												XX	XXX			XX							2.6	
L-17-DK-10												XX	XXX			XX	X						2.6	
L-17-DK-11												XX	XXX			XX							2.6	
L-17-DK-13	XXX					X								XX						XXX			2.7	SITE 3 (2017 ONLY)
L-17-DK-14		XX			XXX			XXX															6.7	SITE 4 2017
L-17-DK-15															XXX								6.7	
L-17-DK-16					XXX	XX									XXX								6.7	
L-17-DK-17														XXX	XX								6.7	
L-17-DK-18		XX	XX		XXX	XX																	6.7	
L-16-DK-16							XX	XX	XX		XX					XXX	XX						6.5	SITE 4 2016
L-16-DK-17	XXX				XX	XX		XXX															6.5	
L-16-DK-18		XX			XX																		6.5	
L-16-DK-19	XXX				XX																		6.5	
L-16-DK-20	XXX				XX	X																	6.5	
L-17-DK-24							XX	XX												XXX			3.2	SITE 5 (2017 ONLY)
L-17-DK-25	XXX	XXX	XX	XX	XXX	XX																	3.2	
L-17-DK-26																						XXX	3.2	
L-17-DK-27	XXX	XXX	XX				XX								XX			XX					3.2	
L-17-DK-28		XX			XX						XX	XX	XXX			XX							3.2	
L-17-DK-31											XX	XXX	XX			XX							NA	GPS POINT 340
L-17-DK-32					XX						XX	XXX	XX			XX							NA	
L-17-DK-34												XX	XXX						XX				3	SITE 6 (2017 ONLY)
L-17-DK-35	XXX				XX		XXX	XX							X					XX			3	
L-17-DK-36	XXX		XX				XX	XXX								XX		XX					3	
L-16-DK-21																						XXX	5	DISCHARGE STREAM
L-17-DK-SUBST	XX				XXX																		NA	SUBSTRATE

Table 3: Mineral phases present in each sample and their relative abundances. XXX = abundant, XX = common, and X = rare. The right column indicates the pH of the adjacent hot spring. Samples collected in 2016 are blue while samples from 2017 are black. The right-most column denotes the site number associated with each sample, and the years in which it was sampled. Halotrichite and pickeringite (Fe^{3+} and Mg^+ endmembers respectively) are indistinguishable in XRD and are both reported as halotrichite.

<u>**XRF**</u>

The samples were analyzed for major and minor elements including Si, Ti, Al, Fe, Mn, Mg, Ca, Na, K, and P (Table 4). Spider diagrams were normalized to the unaltered substrate sample, revealing the patterns of element enrichment and depletion for the samples collected from a variety of hydrothermal features (Figures 17-19). Samples with %LOI above 50% were prepared as pressed pellets to measure sulfur content. Samples prepared as pressed pellets had sulfur concentrations well above the calibrated range of the standards so results could not be used. The composition of the mud samples collected from neutral hot springs is almost identical to the mud collected from the acidic hot springs. The compositions of the altered sediments show more variation between acidic and neutral hot springs and from year to year. Sediments collected from near-neutral hot springs in both years were generally depleted in manganese, magnesium, calcium, sodium, and potassium and relatively unchanged in silica and titanium. Aluminum and iron concentrations were variably enriched and depleted. The acidic sediments from both years were also generally depleted in aluminum, manganese, magnesium, calcium, sodium, and potassium, but they were variably enriched in iron and phosphorous. The sediments collected near acidic sites show two trends for silica and titanium concentrations with one group showing slight enrichment and the other showing slight depletion. Higher silica concentrations are observed for samples containing more abundant silica phases like tridymite. L-17-DK-26 shows strong enrichment in iron and depletion of silica which reflects a lack of any silica phases. The patterns of enrichment and depletion between the acidic and neutral precipitates show that they are geochemically distinct from one another but systematic variation between the two endmembers is not clear.

2016 Fused Bead		SiO$_2$	TiO$_2$	Al$_2$O$_3$	Fe$_2$O$_3$	MnO	MgO	CaO	Na$_2$O	K$_2$O	P$_2$O$_5$	%LOI	Sum	pH
L-16-DK-03	Mud	55.9	0.61	19.45	3.17	0.02	0.67	0.38	0.94	1.58	0.15	15.7	98.78	3.20
L-16-DK-06	Sed	53.38	0.69	27.51	1.00	0.01	0.15	0.19	0.35	1.24	0.18	14.3	99.17	5.40
L-16-DK-07	Sed	85.56	0.62	6.42	1.37	0.01	0.50	0.56	0.74	0.79	0.07	0.40	97.15	5.40
L-16-DK-09	Mud	54.32	0.56	19.72	2.59	0.01	0.40	0.37	0.85	1.53	0.14	18.5	99.11	2.28
L-16-DK-11	Sed	70.47	0.57	0.63	3.33	0.02	0.79	2.63	1.67	1.31	0.09	9.97	100.6	2.28
L-16-DK-12	Mud	74.28	0.50	11.16	1.78	0.01	0.50	1.01	1.37	1.31	0.07	10.9	102.97	2.28
L-16-DK-14	Sed	84.75	0.61	7.23	0.69	0.02	0.39	1.07	1.54	1.32	0.03	2.50	100.29	2.28
L-16-DK-16	Prec	43.83	0.54	22.17	3.53	0.02	1.26	0.23	0.32	0.89	0.39	22.9	95.61	6.50
L-16-DK-17	Mud	60.14	0.79	16.87	5.40	0.03	1.34	2.36	2.51	2.17	0.09	5.57	97.45	6.50
L-16-DK-18	Sed	48.52	0.37	10.05	4.15	0.02	1.14	8.04	1.22	1.44	0.20	21.9	97.46	6.50
L-16-DK-19	Sed	67.14	0.36	8.99	2.92	0.01	0.59	2.59	1.69	1.39	0.08	5.28	97.15	6.50
L-16-DK-20	Sed	80.50	0.53	6.90	0.70	0.01	0.28	0.94	1.36	1.46	0.05	7.00	99.83	6.50
L-16-DK-21	Altered Rock	20.27	0.18	12.66	47.17	0.00	0.28	0.25	0.08	0.25	1.64	14.7	97.84	5.00
2017 Fused Bead														
L-17-DK-02	Mud	54.51	0.62	21.29	4.08	0.03	0.73	1.02	1.23	1.37	0.13	12.10	97.23	6.12
L-17-DK-03	Prec	48.05	0.48	15.94	7.07	0.02	0.54	0.67	0.83	1.13	0.30	19.95	95.14	6.12
L-17-DK-04 Coating	Prec	78.13	0.27	4.36	0.85	0.01	0.49	0.79	0.74	0.67	0.04	13.36	99.79	6.12
L-17-DK-08	Mud	54.26	0.86	15.71	6.27	0.02	0.39	0.47	1.13	1.81	0.11	15.40	96.57	2.65
L-17-DK-13	Mud	45.00	0.60	13.45	4.49	0.02	0.64	0.54	0.92	1.30	0.10	31.00	98.47	2.74
L-17-DK-14	Sed	59.64	0.51	17.8	4.94	0.02	2.04	2.15	1.95	1.86	0.07	6.77	97.89	6.70
L-17-DK-16	Mud	60.47	0.54	17.74	3.83	0.02	1.26	2.11	2.17	1.92	0.09	6.50	96.81	6.70
L-17-DK-18	Sed	71.05	0.58	12.53	2.79	0.01	0.45	1.72	2.50	1.85	0.04	4.97	98.64	6.70
L-17-DK-25	Sed	70.26	0.83	11.42	3.61	0.04	1.27	1.46	1.89	1.81	0.20	5.84	98.84	3.19
L-17-DK-26	Sed	22.02	0.18	7.24	51.78	0.00	0.26	0.15	0.06	0.28	0.92	15.30	98.31	3.19
L-17-DK-27	Prec	49.86	0.24	7.87	22.83	0.01	0.34	0.23	0.20	0.65	0.47	15.60	98.37	3.19
L-17-DK-28	Prec	28.71	0.14	13.13	1.76	0.06	2.10	1.39	2.49	0.77	0.08	47.40	98.10	3.19
L-17-DK-35	Mud	57.61	0.82	15.01	6.39	0.02	0.80	0.49	0.50	0.98	0.12	14.70	97.64	3.02
L-27-DK-36	Prec	62.98	0.74	10.63	8.47	0.01	0.40	0.23	0.47	1.51	0.15	11.90	97.93	3.02
L-17-DK-Sub	Rock	62.11	0.49	16.72	4.41	0.08	2.14	4.54	3.80	1.86	0.11	2.00	98.44	N/A

Table 4: Table of bulk major element composition of Devil's Kitchen hydrothermal altered samples, as measured by XRF and reported as wt% oxide. All Fe reported as Fe$_2$O$_3$, abbreviations: Prec = precipitate, Sed = sediment, Rock = unaltered substrate, Mud = mud sampled below water line, N/A = not analyzed, %LOI = % loss on ignition, pH of closest hot spring is also indicated.
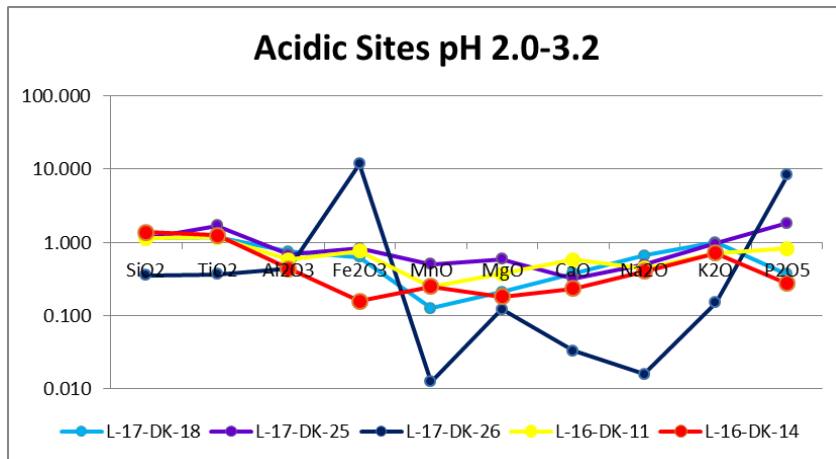
Figure 17: Elemental concentrations of sediment samples collected near acidic hot springs analyzed using the XRF. The elemental concentrations are normalized to the substrate compositions and plotted on a log scale to show enrichment or depletion of an element compared to the substrate composition. All samples show enrichment in SiO$_2$ and TiO$_2$ (except L-17-DK-26, which is anomalously rich in Fe) and uniform depletion in Al$_2$O$_3$ and mobile cations.
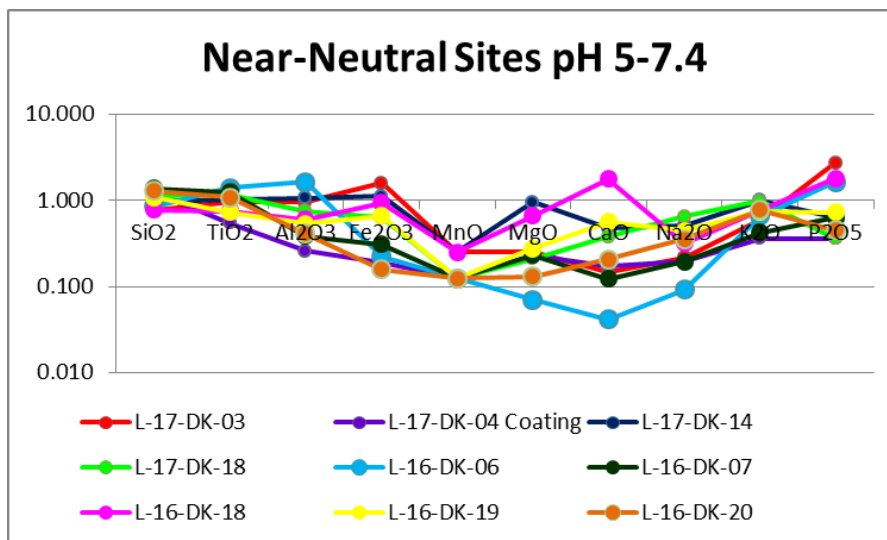

Figure 18: Elemental concentrations of sediment samples collected by near-neutral hot springs analyzed using the XRF. The elemental concentrations are normalized to the substrate compositions and plotted on a log scale to show enrichment or depletion of an element compared to the substrate composition. Samples show variable enrichment and depletion in Al$_2$O$_3$. Samples show depletion in mobile cations except for L-16-DK-18 which has a significant plagioclase component. SiO$_2$ and TiO$_2$ show variable enrichment and depletion.
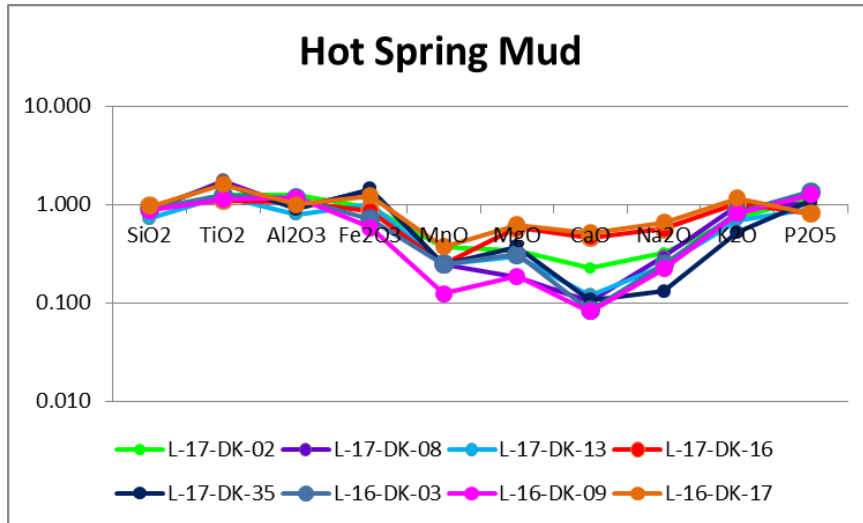
Figure 19: Elemental concentrations of mud samples collected from all hot springs analyzed using the XRF. The elemental concentrations are normalized to the substrate compositions and plotted on a log scale to show enrichment or depletion of an element compared to the substrate composition. Samples are uniformly depleted in mobile cations and enriched in TiO$_2$ while SiO$_2$ concentrations are relatively unchanged or even slightly depleted.

Atomic Adsorption and Ion Chromatography

The samples were analyzed by atomic adsorption (AA) to determine dissolved cation concentrations including Mg$^+$, Ca$^+$, Na$^+$, and K$^+$ and by ion chromatography (IC) to determine dissolved sulfate concentrations (Table 5).

2016	Mg	Ca	Na	K	Sulfate	Phosphate	Nitrate	Chloride	Iron	Bicarbonate	pH
L-16-DK-01	23.85	16.89	6.15	2.61	0.00	0.00	0.00	0.00	N/A	N/A	6.40
L-16-DK-02	20.14	24.28	11.62	4.99	24.40	0.00	0.00	0.00	N/A	N/A	3.20
L-16-DK-08	99.61	249.03	81.91	17.69	150.73	0.00	0.00	0.00	N/A	N/A	2.28
L-16-DK-15	30.62	46.29	16.18	8.20	2.00	0.00	0.00	0.00	N/A	N/A	6.58
L-16-DK-22	24.76	20.37	7.13	3.17	0.00	0.00	0.00	0.00	N/A	N/A	6.63
2017											
L-17-DK-01	4.41	3.03	6.05	1.89	77.01	0.00	0.00	0.00	0.00	0.07	6.12
L-17-DK-06	34.77	70.49	63.97	15.28	1259.02	0.00	0.00	0.00	20.00	1.02	2.65
L-17-DK-12	16.90	29.98	29.93	9.13	551.21	0.00	0.00	0.00	6.00	0.32	2.74
L-17-DK-22	10.68	13.19	26.34	6.22	99.79	0.00	0.00	0.00	0.00	0.10	6.73
L-17-DK-23	16.52	39.28	42.23	14.92	893.93	0.00	0.00	0.00	11.00	0.27	3.19
L-17-DK-29	6.09	2.98	4.86	2.18	8.18	0.00	0.00	0.00	0.00	0.39	6.68
L-17-DK-30	6.21	2.53	4.27	1.83	1.55	0.00	0.00	0.00	0.00	0.12	7.12
L-17-DK-33	8.45	17.26	27.06	11.16	597.28	0.00	0.00	0.00	3.00	0.18	3.02

Table 5: Table of dissolved ion results from the AA and IC analyses. Results reported in parts per million (ppm) and any results below detectable limits are reported as 0. N/A = not analyzed. Iron and bicarbonate concentrations analyzed in the field.

Hydrolab Sonde results showing pH, ORP (oxidation/reduction potential), temperature, TDS (total dissolved solids) and salinity were recorded (Table 6, Figure 20). Concentrations below the detectable limits were reported as zero. High sulfate concentrations correlated with low pH water samples indicating that sulfuric acid is the main acidifying compound in the waters. Calcium and sodium are usually the most abundant dissolved cations with lesser amounts of magnesium and potassium. The more acidic samples tend to have a higher concentration of dissolved cations. Dissolved iron content was measured in situ using CHEMets self-filling ampoules for colorimetric analysis (Iron R-6001). Dissolved iron concentrations, ranging from 0-20 ppm, show a strong positive correlation with relative sulfate concentration (Figure 21).

Hydrolab Results								
	pH	ORP	T (insitu)	T (HL)	TDS	Salinity psu	Conductivity	DO
2016	(HL)	mV	°C	°C	g/L	ppt	µS/cm	mg/L
L-16-DK-01	6.80	263	9.30	9.37	0.10	0.07	108.30	N/A
L-16-DK-02	3.20	277	90.90	46.00	0.39	0.30	915.30	N/A
L-16-DK-05	5.40	335	92.00	47.00	0.13	0.10	297.20	N/A
L-16-DK-08	2.28	590	80.40	37.47	2.29	1.82	4395.50	N/A
L-16-DK-15	6.58	120	88.40	35.04	0.20	0.15	380.20	N/A
L-16-DK-22	6.63	190	15.40	15.31	0.11	0.08	136.40	N/A
2017								
L-17-DK-01	6.12	11	88.10	44.82	0.11	0.09	233.20	0.47
L-17-DK-06	2.65	417	77.00	41.81	1.34	1.08	2873.30	0.71
L-17-DK-12	2.74	495	88.90	37.28	0.85	0.66	1662.90	0.32
L-17-DK-22	6.73	26	83.00	43.89	0.18	0.14	402.70	0.04
L-17-DK-23	3.19	566	85.00	49.93	0.69	0.55	1690.20	0.00
L-17-DK-29	6.68	198	16.40	15.33	0.09	0.07	114.60	6.29
L-17-DK-30	7.12	261	10.90	10.65	0.08	0.06	96.50	7.08
L-17-DK-33	3.02	467	85.80	35.67	0.53	0.41	1013.10	0.38

Table 6: Table of results from the Hydrolab Sonde analysis. The pH is shown as measured by the Hydrolab, ORP = oxidation/reduction potential, T (insitu) was measured using a digital thermometer in the hot spring prior to sampling and cooling, T (HL) was measured using the Hydrolab after allowing the water to cool below 50°C, TDS = total dissolved solids, and DO = dissolved oxygen. DO was not measured in 2016 because the sensor was broken.
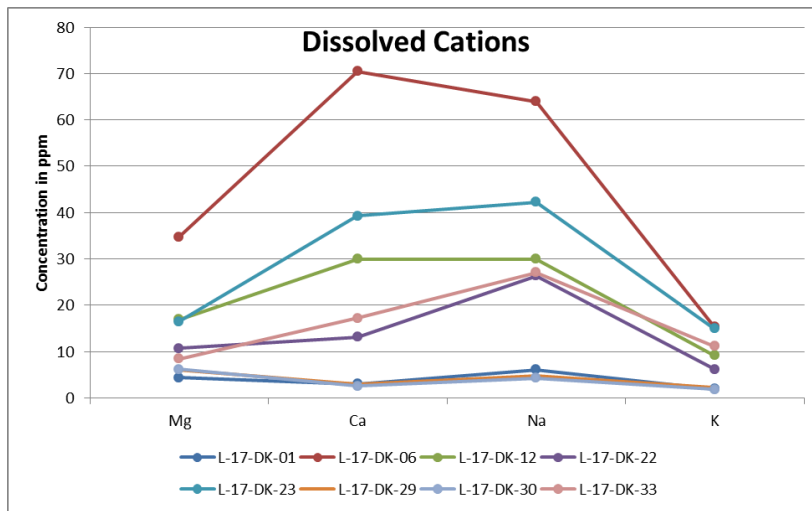

Figure 20: Dissolved cation concentrations of water samples collected in 2017. Each colored line represents a single water sample. The colors and sample numbers are the same as the next figure. L-17-DK-29 and L-17-DK-30 are non-thermal stream water samples collected downstream and upstream from the hydrothermal area respectively.
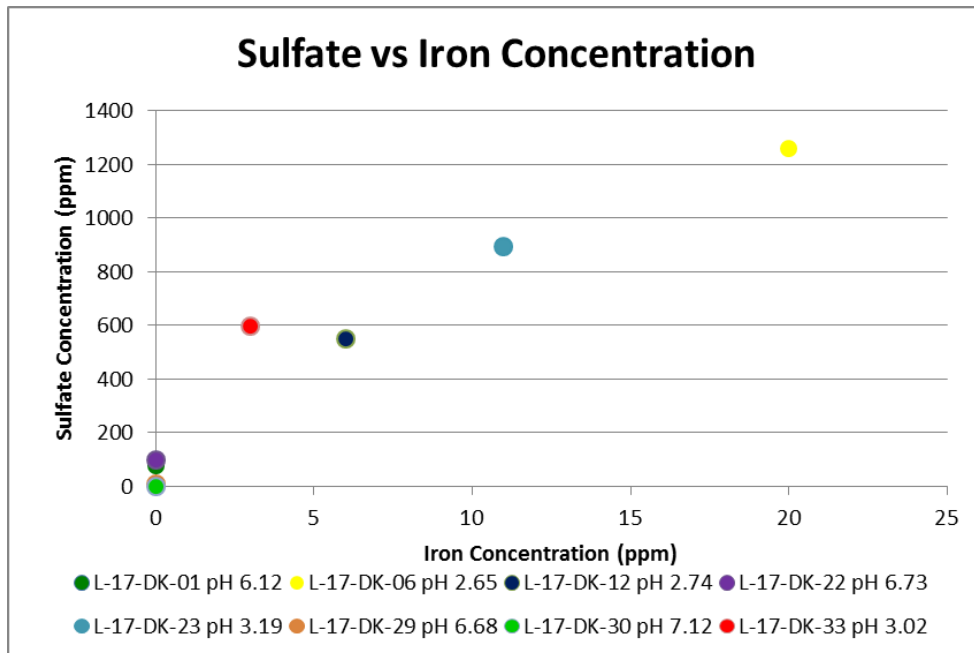
33

Figure 21: Bivariate plot sulfate vs iron concentration for water samples collected in 2017. There is a strong positive correlation between sulfate and iron concentration. Samples L-17-DK-29 and L-17-DK-30 are non-thermal stream water samples while the rest are hot spring samples.

SEM

Two silica-rich samples collected in 2017 (L-17-DK-04 and L-17-DK-27) were analyzed by SEM. Both were analyzed using a secondary electron detector and an energy dispersive x-ray spectroscopy system (EDS). Secondary electron analysis was conducted to find and image any biological structures present in the samples, and also revealed the relative crystallinity of the sample and the shape of the crystalline minerals present. The EDS analysis aided in mineral identification and allowed for qualitative elemental mapping.
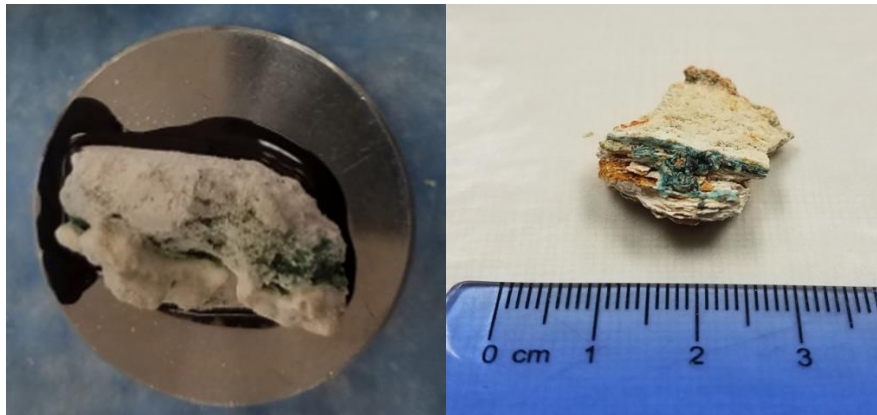
Figure 22: Left: one of six pieces cut from sample L-17-DK-04 collected from a near-neutral site (pH 6.12). The sample was composed of the lobate white material with areas covered in fuzzy green material. Right: sample L-17-DK-27 collected from an acidic site (pH 3.19). The sample consists of whitish tan and rusty orange layers with teal and green material on one end.

Samples collected from the neutral (sample L-17-DK-04) and acidic (sample L-17-DK-27) hot springs were analyzed by SEM because they incorporated a fuzzy green material interpreted as algae or cyanobacteria (Figure 22). The sample from the acidic site (L-17-DK-27) was a thin, laminar piece of rust colored sediment interlayered with lighter colored layers and coated in green algae. L-17-DK-27 was collected from right on the water line and the bottom of the sample was in contact with the water. The sample collected from the near-neutral site (L-17-DK-04) was a thin lobate coating on a rock sample. The rock sample was partially submerged in the hot spring and the lobate, white silica coating was on the portion that was above the water line. The white, lobate coating on the rock had algae incorporated into it. The SEM analysis of L-17-DK-04 revealed a generally crystal-poor substrate. L-17-DK-04 was comprised predominantly of amorphous silica while L-17-DK-27 was comprised of a mixture of crystalline silica phases, clay minerals, and sulfates. Much of the substrate of L-17-DK-04 was coated in small (<1 micron) globs of amorphous silica. Some of the larger blocks of amorphous silica substrate appear embayed with a Swiss-cheese-like texture indicating that they are being

dissolved in some way. Both samples contain abundant biological structures including rod-shaped microbes, algae, pollen, diatoms, phytoplankton and biofilms (Figures 23-26); additional images of biological structures are shown in the appendix (Figure 42). The microbes were often found in etch pits and with EPS (extra polymeric substance; natural polymers rich in carbon and of high molecular weight secreted by microorganisms) nearby (Staudt et al., 2004). Rod shaped microbes, usually 1-2 microns in length, were often covered in tiny globules of amorphous silica and incorporated into the amorphous silica substrate. In some places the microbes were abundant, with 40-50 microbes in a 100 micron diameter field of view. The fuzzy green material observed in the hand sample is comprised of algal cells which were usually found in relatively large colonies often associated with microbes and EPS. The algae cells were generally spherical and where cell cross sections were visible, a separate cell wall and intercellular material could be distinguished. A few areas were observed where the algal cells were caught in the middle of cell division. Pollen grains were found attached to the substrate and coated in amorphous silica. The pollen grains observed likely came from the plant life surrounding the hydrothermal area (rather than from the algae cells within the sample) and fell in and were incorporated into the silica coating. Phytoplankton like diatoms and dinoflagellates were also found in the silica samples and were often remarkably well preserved (Figure 25). Both types of phytoplankton were found with amorphous silica globules on them. Rounded mound shaped biofilms were also observed (Figure 26). These biofilms were carbon-rich and had a texture reminiscent of a brain; they were globular and lobate structures with lots of stringy material connecting everything together. The biofilm mounds often had rod shaped microbes and elongated filamentous structures attached to them.
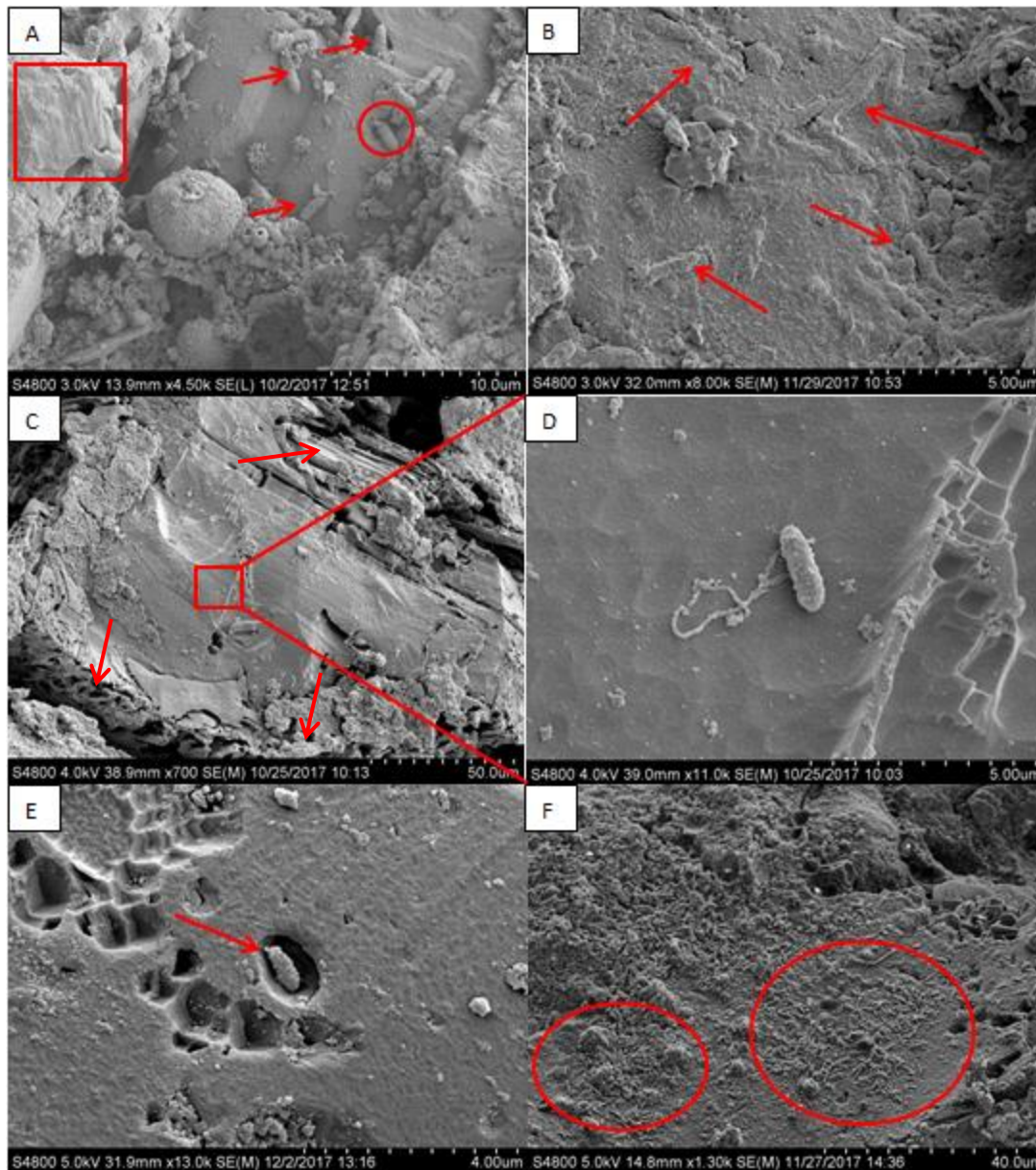
Figure 23 A-F: Panels A-F are from sample L-17-DK-04. (A) Rod-shaped microbes indicated by the red arrows. The etch pit circled in red hosts a rod-shaped microbe. The red box shows an area covered in EPS (extra polymeric substance) likely secreted by the rod-shaped microbes. (B) The red arrow show rod shaped microbes being incorporated into the substrate. They are covered in globules of amorphous silica. (C) A relatively large block of amorphous silica that has embayed edges (shown by red arrows), showing that it is being dissolved. (D) Inset from image C showing a rod-shaped microbe with a string of EPS still attached to it. (E) A rod shaped microbe in its associated etch pit. (F) Two large colonies of rod-shaped microbes circled in red. Each colony consists of at least 30-40 individual microbes.
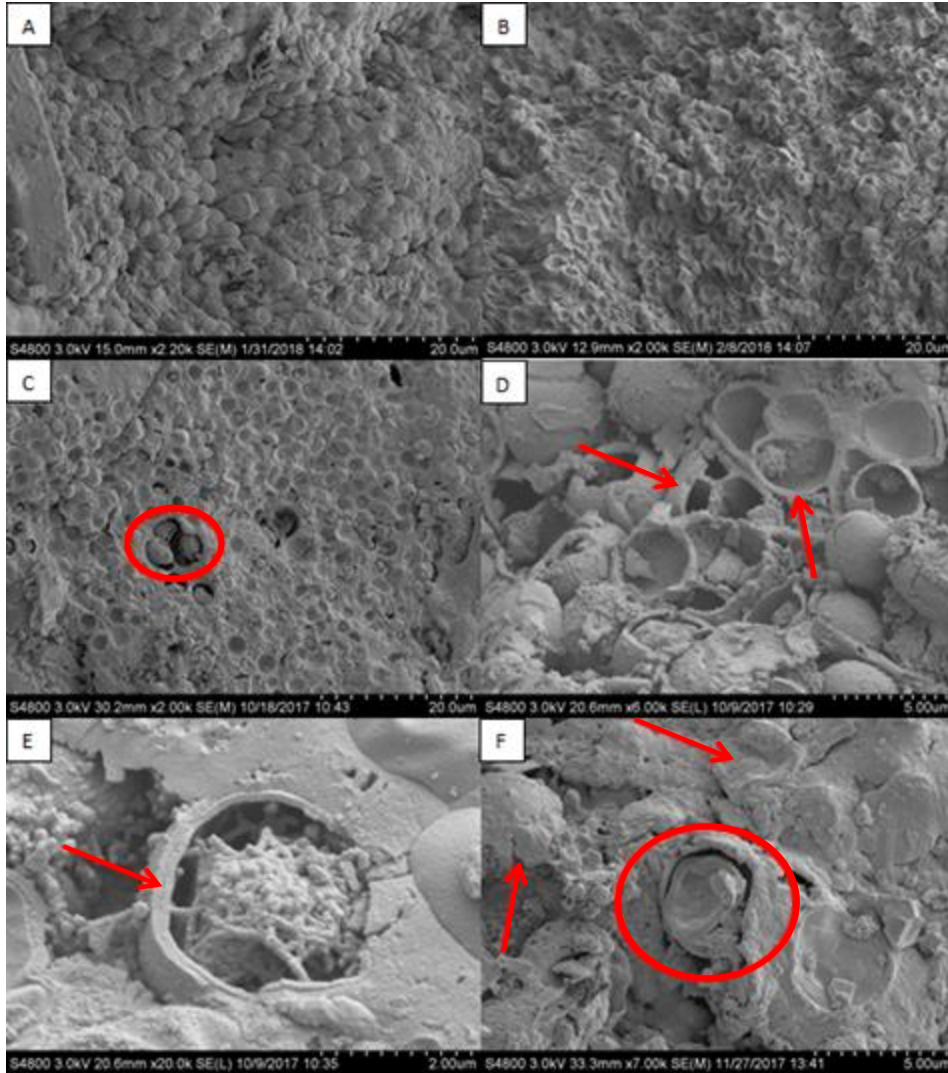
Figure 24 A-F: Panels A and B are from sample L-17-DK-27 and panels C-F are from L-17-DK-04. (A) A large region covered in sub-spherical algae cells with ropy texture and furrowed surfaces. **(B)** Another region covered in a colony of algae cells with a different morphology. The algae cells are biconcave and often oval shaped. **(C)** Large areas are covered by a honeycomb texture where spherical algae cells have fallen off the substrate. The red circle shows an area with three-fold symmetry where algae cells were caught in the middle of cell division. **(D)** Sub-spherical algae cells with cross section visible, showing three separate cells connected at the center indicating that it was in the middle of cell division. **(E)** Algae cell with cross section visible showing intercellular material and a two-layered cell wall. The red arrow points at the two distinct cell wall layers. **(F)** The red circle shows a biconcave shaped algae cell that has been broken open leaving a visible cross section, revealing a distinct cell wall and intercellular material. The red arrows show mounded structures that are likely other algae cells covered in amorphous silica.
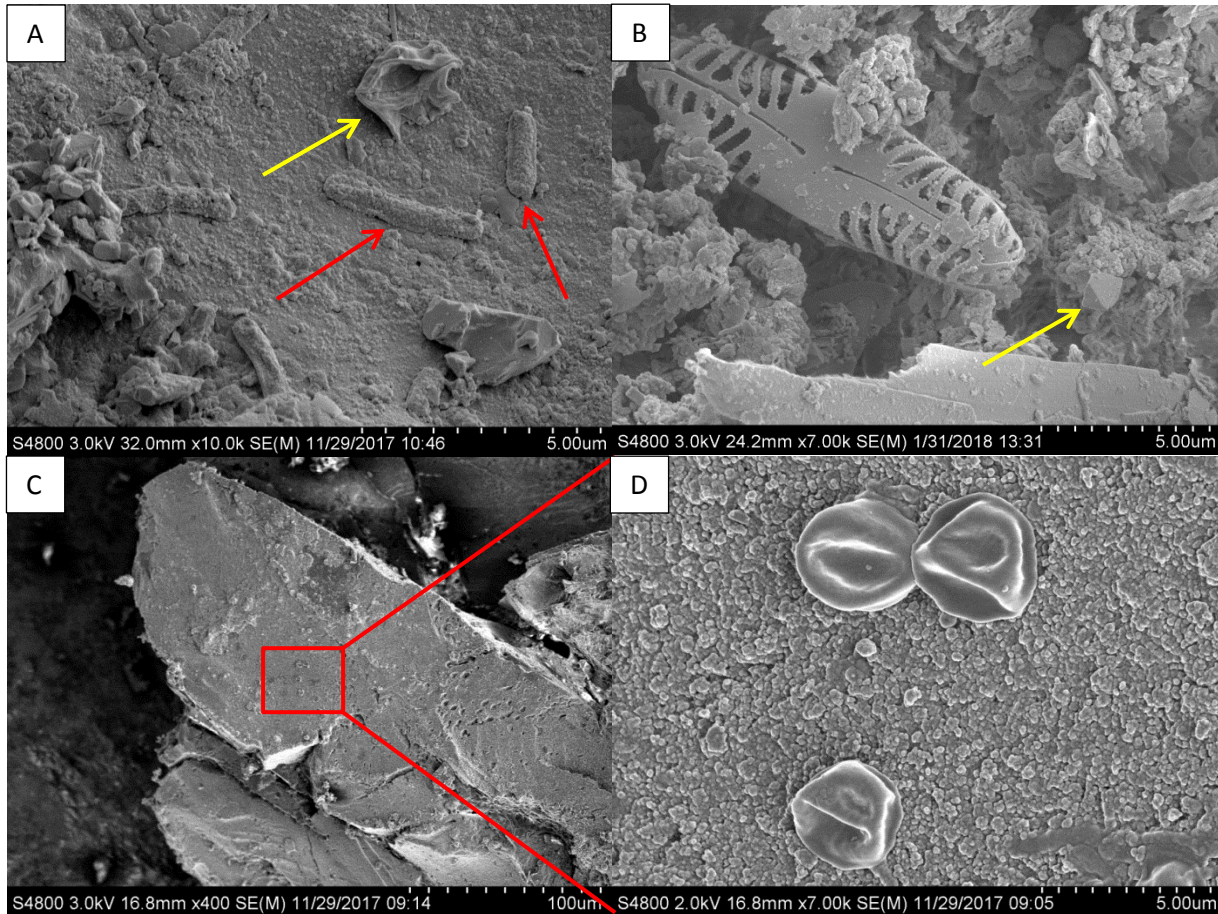
Figure 25 A-D: Panels A, C, and D are from sample L-17-DK-04 and panel B is from L-17-DK-27. (A) The red arrows shows rod-shaped microbes that are covered in tiny globules of amorphous silica. The yellow arrow shows a phytoplankton called a dinoflagellate. (B) A well-preserved diatom frustrule. The diatom is surrounded by silica globules and minor amounts of crystalline material. The yellow arrow shows an octahedral alunite crystal. (C) A large block of amorphous silica, with an inset showing a higher magnification image. (D) Inset image showing three subspherical pollen grains sitting on the silica substrate.
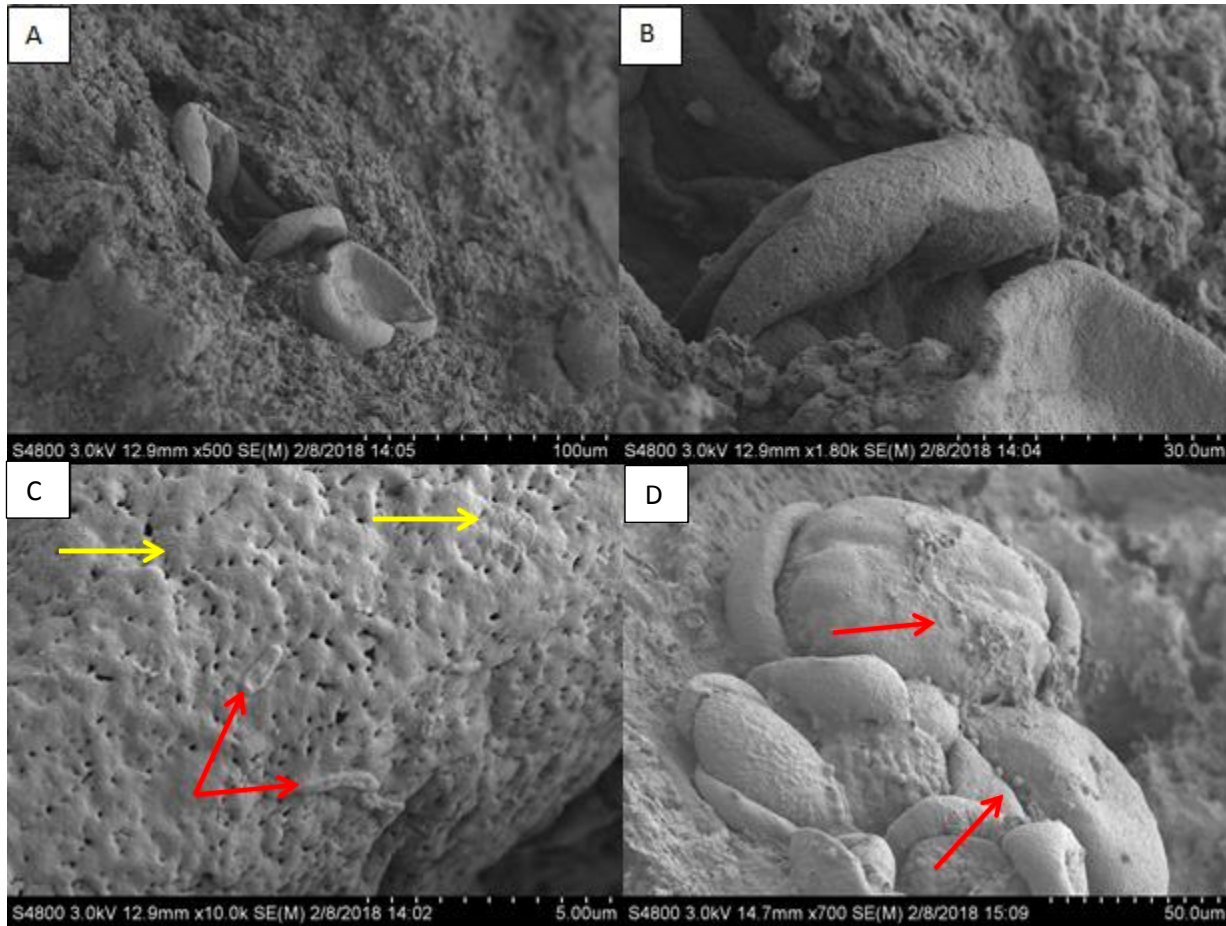
Figure 26 A-D: Panels A-D from sample L-17-DK-27. (A) Lobe-shaped biofilms attached to the silica substrate. (B) A higher magnification image of the same lobe-shaped biofilm. (C) A high magnification image of the same biofilm showing the lobate texture of the biofilm that is reminiscent of a brain. The red arrows point to rod-shaped microbes attached to the biofilm. The yellow arrows point to thin filamentous structures that are common on the biofilm. (D) A different, large lobate biofilm with small spherical structures attached to it. The red arrows point out the spherical structures.

EDS analysis aided in mineral identification and helped determine the elemental composition of the biological structures. The samples were dominantly composed of amorphous silica with minor crystalline phases. Minor crystalline phases identified include gypsum, alunite, and other unidentified crystalline material (Figure 27). EDS analysis of an algal colony revealed that the algae cells were predominantly made of silica. There was often

40

carbon-rich EPS associated with the margins of the algal colonies (Figure 28). There were other algae morphologies that were carbon rather than silica-rich. Microbes were indistinguishable from the background amorphous silica and did not show any identifiable chemical signature. The diatoms analyzed were predominantly made of silica. The biofilms and algae analyzed were composed of carbon and were attached to the siliceous substrate (Figure 29). Additional EDS images showing more mineral and algae species shown in Appendix (Figures 43-46).
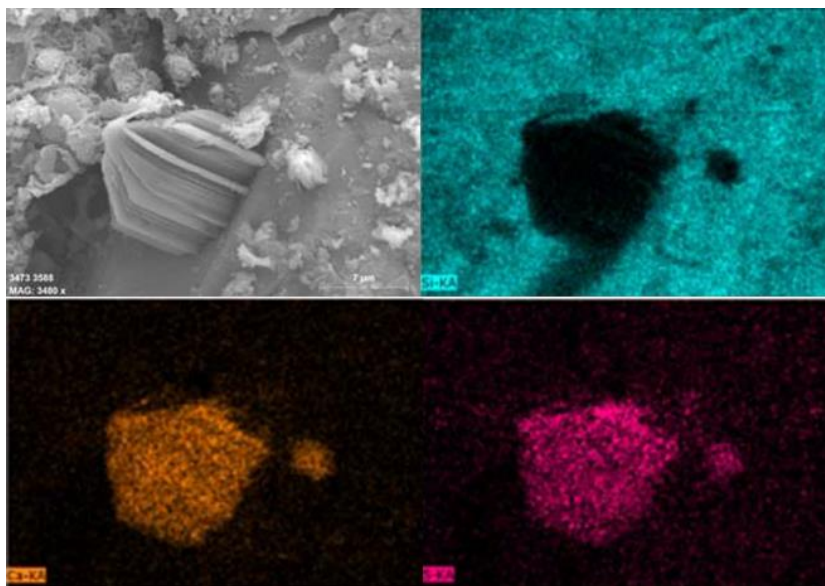

Figure 27: EDS elemental maps of a gypsum crystal from L-17-DK-04. The crystal contains no silica (teal), and it is rich in calcium (orange) and sulfur (pink). This is consistent with a gypsum crystal (CaSO$_4$*2H$_2$O).
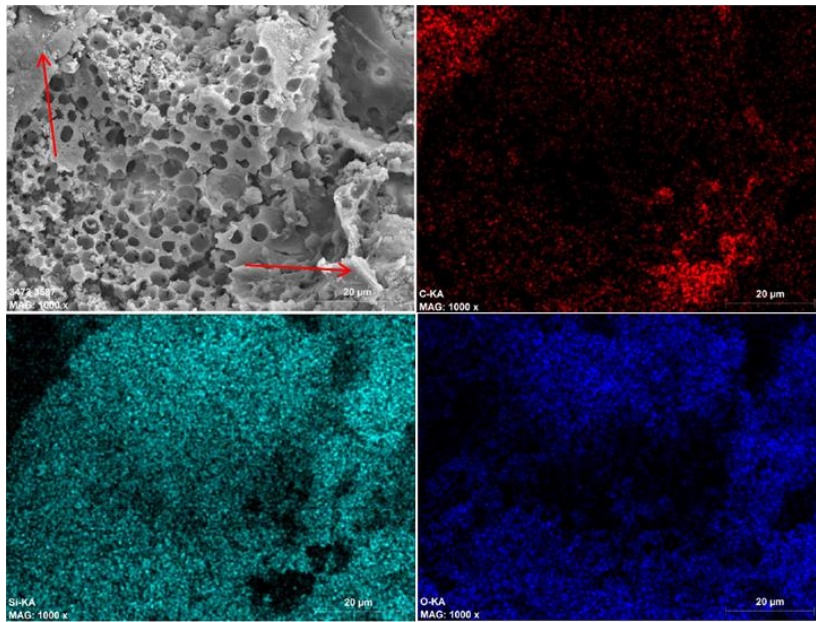
Figure 28: EDS elemental maps of sample L-17-DK-04 of an area covered by spherical algae cells. There are two carbon-rich areas (red arrows) made of EPS. The area covered by the algae cells is silica-rich, suggesting that these are siliceous algae.
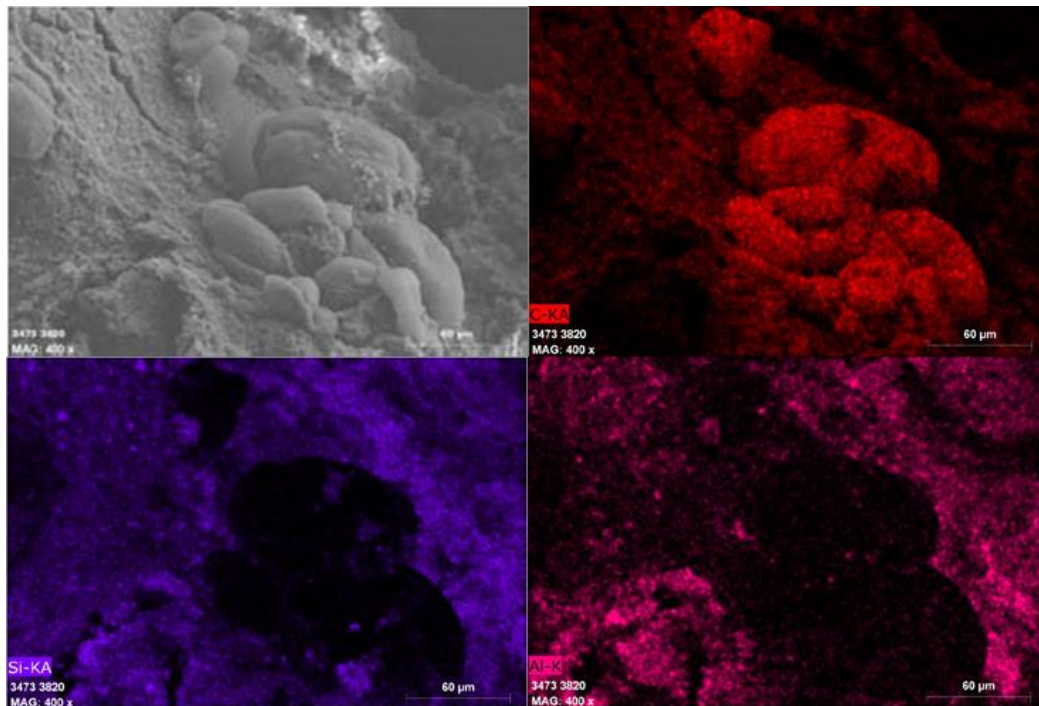

Figure 29: EDS elemental maps of sample L-17-DK-27 of a group of lobate biofilms. The analysis shows that the lobate biofilms have a high concentration of carbon compared to the surrounding substrate and are deficient in silicon and aluminum compared to the substrate.

Discussion

Mineralogy Discussion

The hydrothermal system at Devil's kitchen yields a diverse mineralogical suite including silica phases, primary igneous phases, clay minerals, and sulfates. Primary igneous phases including plagioclase, potassium feldspar, tridymite, and cristobalite are present in both acidic and neutral hydrothermal environments, and primary phases reflect the original dacitic composition of the substrate. Primary minerals are concentrated in the mud samples collected because the hydrothermal muds are composed of sediments derived from the local substrate in addition to more recent hydrothermal precipitates. Native sulfur was observed in one mud sampled collected from an acidic (pH of 3.5) hot spring. The presence of native sulfur indicates more reducing conditions compared to other springs, which contain sulfates. Sulfide phases were generally not observed.

The dominant silica phase present was tridymite with lesser amounts of cristobalite. This probably represents either a magmatic phase or a relict phase from an earlier, hotter hydrothermal system (Figure 30) because the current system doesn't reach high enough temperatures to convert silica to tridymite (Kuniaki et al., 1987). Tridymite forms at 870-1470 °C, which is a much higher temperature than the current hydrothermal system.
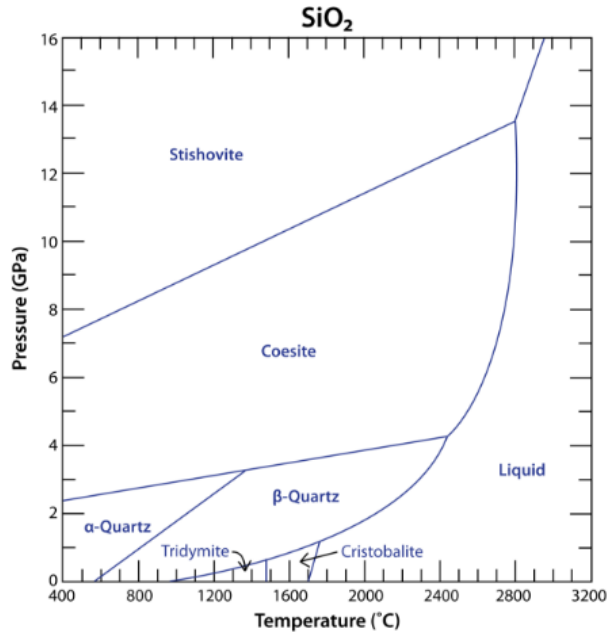
Figure 30: Pressure-temperature phase diagram for SiO₂ showing the stability field for different silica phases. Tridymite is stable between ~870-1470°C. Adapted from Winter 2010.

Amorphous silica is present in four samples, three of which are from site 1 which is a near-neutral hot spring. The amorphous silica was found as a coating on an altered rock sample (analyzed by SEM) and had biological structures incorporated within. Two samples (L-16-DK-07 and L-17-DK-04) that had amorphous silica had relatively high concentrations of silica and relatively low concentrations of titanium. This decoupling of the silica and titanium concentrations suggests that the amorphous silica is the product of direct precipitation, rather than the product of acid-sulfate leaching, which tends to concentrate both silica and titanium together (e.g. McHenry et al., 2017).

Sulfate minerals are present at both acidic and near-neutral hot springs but the specific sulfate phases present are more variable. Aluminum sulfates are the dominant sulfate phase present and are present at all hot springs. The presence of specific sulfate phases can be

44

indicative of the environmental conditions at each site. For example, jarosite is an Fe^{3+} mineral and is an indicator of more oxidizing conditions. It was found near three different hot springs, which had high ORP values (590, 566, and 467 mV) and low pH waters (2.28, 3.19, and 3.02 respectively) (Figure 31). The presence of jarosite is good evidence for more oxidizing conditions and a relatively low pH. Alunogen, halotrichite, tamarugite, gypsum, and alunite (Al^{3+}, Fe^{3+}, Na^+, Ca^{2+}, and K^+ sulfates, respectively) are the most common precipitates observed. The aluminum, sodium, calcium, and potassium components are likely available from leaching of primary feldspar minerals. These constituents could be mobilized by the water, combined with the sulfate dissolved in the water, and precipitated around the hot spring, and could help explain why sulfates containing these anions are the most abundant precipitates around the hot springs. Iron sulfates are also common around the hot springs. The Fe^{3+} was likely leached from less abundant biotite and hornblende in the substrate and combined with sulfate ions in the water and precipitated as before.
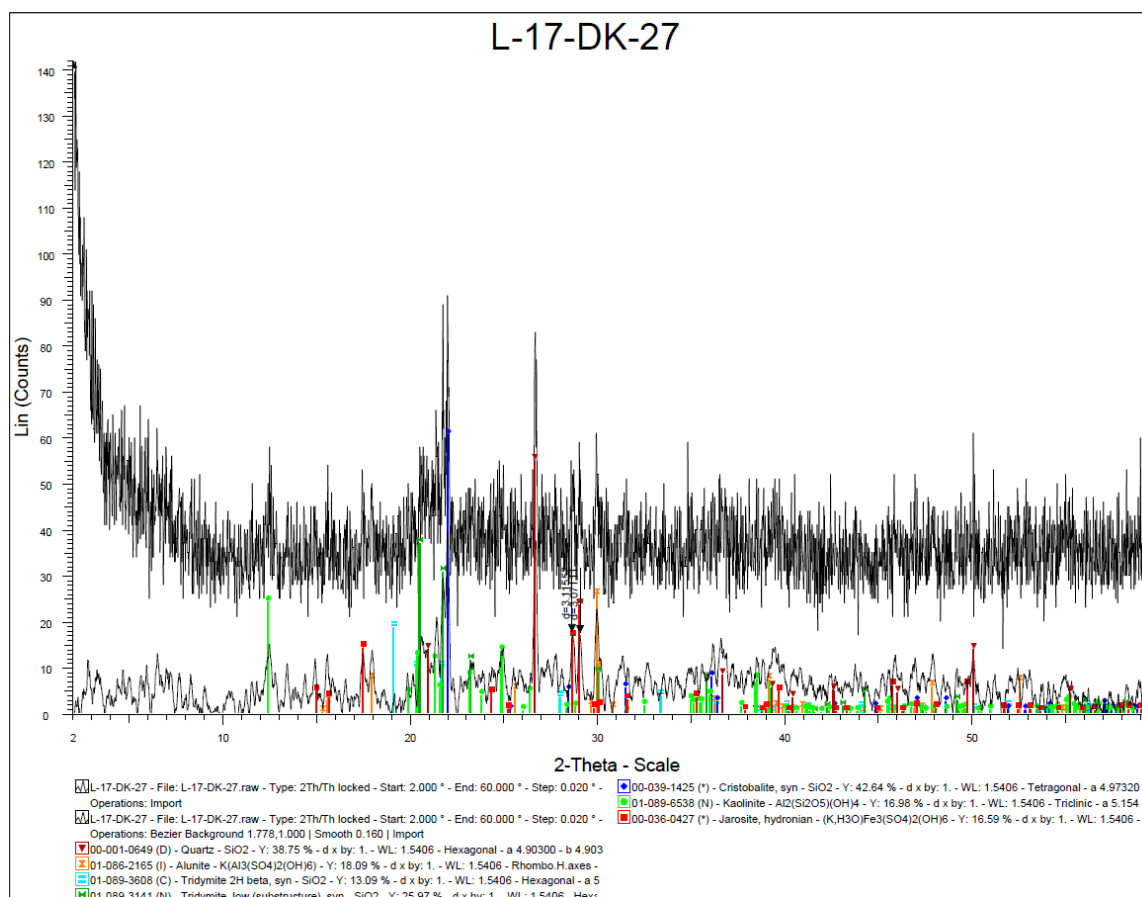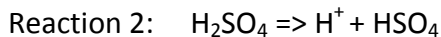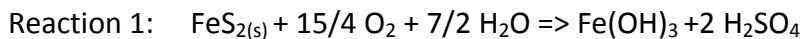
Figure 31: XRD pattern for L-17-DK-27 showing one of the samples analyzed using SEM. Pattern showing presence of jarosite. The elevated background signal is likely associated with iron fluorescence. The top pattern shows the unaltered XRD scan and the lower pattern shows the same scan with background subtracted and smoothed. This sample was collected from a hot spring with a pH of 3.19 and ORP of 566 mV.

Sulfides are conspicuously absent at Devil's Kitchen. Pyrite was the only sulfide identified and it was a minor constituent in one sample (L-17-DK-04-Coating). The lack of sulfide phases is expected due to the predominantly oxidizing conditions, but this demonstrates how the presence or absence of certain mineral phases can be used to help understand the environmental conditions at the time of deposition. Sulfides are abundant at other sites at Lassen (e.g. Little Hot Springs Valley, Bumpass Hell), where lower ORP values were observed locally (e.g. McHenry et al., 2017).

<u>Water Chemistry Discussion</u>

Dissolved anion concentration results (Table 5) show that high sulfate concentrations correlate with low pH, indicating that the sulfate concentration is the main control on the pH of the water. Water samples with lower pH generally had a higher concentration of dissolved cations as well which is consistent with the more acidic waters dissolving the plagioclase-rich rocks with which they are in contact.

Dissolved cation concentration plots show that calcium and sodium are usually the most abundant dissolved cations with lesser amounts of magnesium and potassium. The dissolved iron and sulfate concentrations covary (Figure 21). The low pH hot springs are more oxidizing than the more neutral hot springs so the sulfate concentrations and the iron concentrations could be related by the oxidation of pyrite at depth through the following reaction 1 (after McHenry et al., 2011). The sulfuric acid would then dissociate in water through the following reaction 2 and 3.

Reaction 1: $FeS_{2(s)} + 15/4\ O_2 + 7/2\ H_2O => Fe(OH)_3 + 2\ H_2SO_4$

Reaction 2: $H_2SO_4 => H^+ + HSO_4$

Reaction 3: $HSO_4 => H^+ + SO_4$

These reactions would produce sulfate ions and iron ions in solution and drive the pH of the water down, which is consistent with our observations. This mechanism would require a mass of pyrite to be oxidized. XRD analysis only showed a minor amount of pyrite present in one sample, so if there is pyrite being oxidized it is either at depth underneath the

hydrothermal system, or it was not sampled. Pyrite and other sulfide minerals are abundant at other hydrothermal sites at Lassen (e.g. Little Hot Springs Valley, Bumpass Hell) where ORP values are lower (e.g. McHenry et al., 2017).

Geochemistry Discussion

Major element concentrations show that minor leaching occurs in both acidic and near-neutral environments. The mud samples collected from acidic and near-neutral hot springs are all uniformly depleted in MgO, MnO, CaO, Na_2O and K_2O whereas TiO_2 (a more immobile element) is enriched in all samples. Mud samples can be enriched or depleted in Al_2O_3, Fe_2O_3, and P_2O_5 while silica concentrations are almost unchanged (Figures 17-19). This is consistent with open-system acid-sulfate leaching with a high water-rock ratio which removed the more mobile cations from the system, residually enriching titanium (e.g. McHenry et al., 2017). The mud samples collected from acidic and near-neutral environments show the same general geochemical trend of depletion in more mobile cations and residual enrichment (or unchanged concentrations) of less mobile elements like titanium, silica, and aluminum. This is consistent with the water chemistry of the hot springs. The water samples collected from the hot springs had high concentrations of more mobile cations (Mg^{2+}, Ca^{2+}, Na^+, and K^+). In general, more acidic hot springs have higher concentrations of dissolved ions (Figure 20). This shows that the water leaches the mobile cations while residually enriching the mud in the hot springs with more immobile elements like TiO_2.

Geochemical trends for altered sediments show differences between acidic and near-neutral conditions. Sediments from acidic environments are uniformly depleted in Al_2O_3, MnO, MgO, CaO, Na_2O, and K_2O. Most acidic sediments are depleted in Fe_2O_3 with L-17-DK-26 being

48

the only exception. This sample yielded high backgrounds and no diffraction peaks in its XRD pattern, consistent with high iron concentrations (causing iron fluorescence), possibly in the form of a non-diffracting nanophase iron oxide or hydroxide (Figure 39). Acidic sediments are variably enriched and depleted in SiO_2, TiO_2, and P_2O_5. Acidic sediments with SiO_2 enrichment all contain tridymite. Near-neutral sediments show similar trends to the acidic sediments for SiO_2, Fe_2O_3, MnO, MgO, CaO (except for L-17-DK-18 due to abundant plagioclase), Na_2O, K_2O, and P_2O_5 but show a different trend for Al_2O_3. Near-neutral sediments are variably enriched or depleted in Al_2O_3. Near-neutral samples with Al_2O_3 enrichment have a significant kaolinite component. The amorphous silica coating sample (L-17-DK-04-Coating) had a high concentration of silica and a low concentration of titanium. This decoupling of the silica and titanium concentrations suggests that the amorphous silica is the product of direct precipitation from a silica rich fluid, rather than the product of acid-sulfate leaching, which tends to concentrate both silica and titanium together (e.g. McHenry et al., 2017). One sample (L-17-DK-25) from an acidic hot spring that also contained amorphous silica showed a different trend. L-17-DK-25 showed enrichment in both silica and titanium concentrations, which suggests that the amorphous silica in L-17-DK-25 is the product of acid-sulfate leaching (Figure 32).
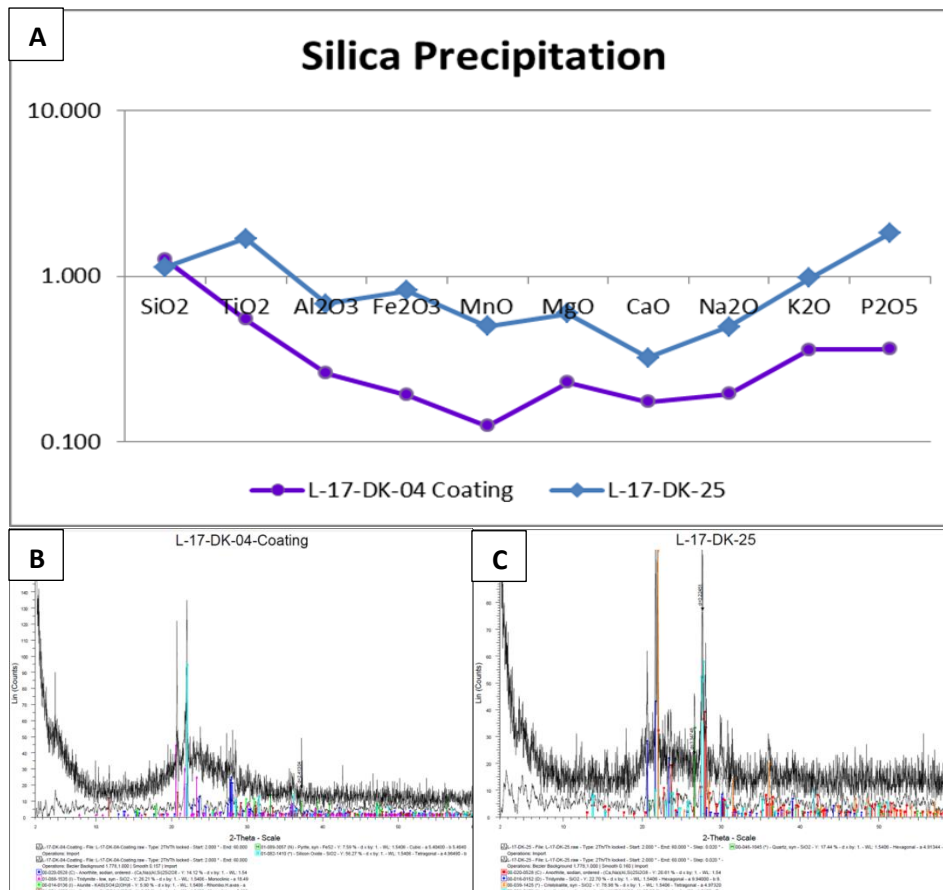
Figure 32: (A) Spider diagram showing a decoupling of the silica and titanium concentrations for near-neutral amorphous silica rich sample L-17-DK-04 Coating and residual enrichment of silica and titanium concentrations for the amorphous silica rich sample from an acidic environment L-17-DK-25. **(B)** XRD pattern for L-17-DK-04 Coating showing an amorphous silica hump. The top pattern shows the unaltered XRD scan and the lower pattern shows the same scan with background subtracted and smoothed. **(C)** XRD pattern for L-17-DK-25 showing an amorphous silica hump. The top pattern shows the unaltered XRD scan and the lower pattern shows the same scan with background subtracted and smoothed

Mud samples from acidic and near-neutral hot springs are geochemically indistinguishable from each other. Altered sediments show more variation between acidic and near-neutral environments but are still relatively similar. Sediments from acidic and near-neutral environments show geochemical trends consistent with minor acid-sulfate leaching with residually enriched silica and titanium. Near-neutral samples can be enriched in Al_2O_3 due

to the kaolinite component while the acidic samples are uniformly depleted in aluminum, but the difference is relatively small. Two sediment samples from acidic environments (L-17-DK-26 and L-17-DK-27) and one from a near-neutral discharge stream (L-16-DK-21) are significantly enriched in Fe_2O_3 compared to the other samples. This is likely because of the presence of Fe-sulfates and/or an iron-rich phase not detectable by XRD causing an elevated background pattern due to iron fluorescence (possibly a nanophase iron oxide or hydroxide). The altered sediment samples do show geochemical variation between acidic and near-neutral environments, but the variation is small and not uniform for every site.

Biosignatures in Hot Springs

Hydrothermal environments provide the components necessary for life to exist: heat, water, and the chemical components for chemosynthesis (Yen et al., 2008). This makes hydrothermal environments, particularly near-neutral sinter depositing environments, an ideal location to look for evidence of life on other planets. Sinters preserve biosignatures of past environments because the rapidly precipitating silica coats all surfaces, including microbes living in the environment (Lynne et al., 2006). Amorphous silica coatings were found on two samples collected at Devil's Kitchen from acidic (pH 3.2) and near-neutral (pH 5.0) environments.

Both samples had abundant biological structures incorporated into the silica coating (rod-shaped microbes, algae, diatoms, phytoplankton, pollen, and biofilms). The abundant biological structures observed demonstrate the habitability of both the acidic and near-neutral environments. The rod-shaped microbes observed in L-17-DK-04 were found in dissolution etch pits and associated with EPS, which indicates that they are actually living on the substrate and

51

metabolizing it. The microbes are often observed covered in tiny globs of silica coating their bodies. Rapid precipitation of silica covers the biological structures and creates a high preservation potential, making them useful biosignatures. The rapid precipitation of silica can also preserve biological structures that are not directly associated with the hot spring itself (e.g. pollen grains in (Figure 25) which means any biological structures from the surrounding area could be incorporated into the precipitating silica and be preserved.

The biological structures varied between the acidic and near-neutral hot springs. The silica coating from the near-neutral hot spring had a wider diversity of biological structures including rod-shaped microbes, siliceous algae, and phytoplankton. The more neutral hot spring is a less harsh environment for the rod-shaped microbes to live in. The sample from the acidic hot spring had no rod-shaped microbes, but it did have biofilms and multiple algae morphologies present. It still represented a habitable environment, but showed lower diversity and abundance.

Comparisons to Mars

The Devil's Kitchen hydrothermal site can be a useful analogue for the proposed hydrothermal site at Home Plate because mineralogical and geochemical patterns can be studied over the wide range of hydrothermal conditions in a small area. Direct comparison is difficult because of the different substrate compositions. The substrate at Devil's Kitchen is dacitic which has a much higher SiO_2 content and Al_2O_3 content than the high-Fe basalt composition of Mars (e.g. L-17-DK-Sub with 62.11 wt% SiO_2 and 16.72 wt% Al_2O_3 compared to Barnhill class rock named Ace with 45.2 wt% SiO_2 and 8.91 wt% Al_2O_3) (McSween et al., 2006 and Squyres et al., 2007). The patterns of relative elemental enrichment and depletion at

Devil's Kitchen should still be similar to Home Plate because the processes controlling element mobility should be similar on both planets. Direct comparison is also complicated by the different atmospheric compositions of Mars and Earth and the abundance of water on Earth compared to Mars. These differences will likely result in: more abundant aluminum sulfates at Lassen than on Mars; better preservation of soluble phases on Mars due to the lack of precipitation and surface water; and opal-A being the dominant silica phase present on Mars due to the lack of diagenetic maturation due to colder, drier conditions (McHenry et al., 2017).

Near Home Plate, Spirit observed silica-rich nodular outcrops, soils that were rich in silica, and other soils that were rich in sulfates. The silica-rich nodular outcrops (e.g. Elizabeth Mahon target) have a digitate or lobate morphology which is very similar to the amorphous silica precipitates at Devil's Kitchen (Figure 33).

Figure 33: Side-by-side comparison of amorphous silica precipitate sample L-17-DK-04 Coating (left) from Devil's Kitchen and the Elizabeth Mahon Target from Home Plate (right). Both samples have a similar lobate morphology with regions of a smooth texture and regions of a more porous texture. The black scale bars at the bottoms of both images is ~2.5 cm.

The silica-rich outcrops and soils around Home Plate range from ~65-92 wt% SiO_2 while the original Martian soil compositions are ~48 wt% SiO_2 (Ruff et al., 2011). These high silica materials show a significant enrichment in SiO_2 relative to local basalts. The Elizabeth Mahon class rocks, located in a local low called Eastern Valley southeast of Home Plate, had ~61-72 wt% SiO_2 and are relatively depleted in Al and Mg compared to the basaltic substrate (Ming et al., 2008). This depletion in Al and Mg suggests that either silica is being retained while Mg and Al are being removed, or that Mg and Al are being removed faster than silica (Ming et al., 2008). There is a much less significant change in wt% SiO_2 at Devil's Kitchen. The hot spring mud samples usually show minor depletion in SiO_2 or no change at all when compared to the substrate. The altered sediment samples are more variable and show both minor enrichment and minor depletion, depending on the sample. Samples showing silica enrichment usually have a crystalline silica phase present like tridymite. Tridymite has been identified in silica-rich mudstones at Gale crater by the Mars Science Lab Curiosity, but it is not a common mineral phase on Mars like it is at Devil's Kitchen due to the relative lack of silicic volcanism on Mars (Morris et al., 2016). The highest SiO_2 concentration measured was in the silica coating sample L-17-DK-04 which had 78.13 wt% SiO_2. The elevated SiO_2 concentrations in the silica-rich outcrops and soils around Home plate are thus much more significant than the SiO_2 enrichment at Devil's Kitchen in the hot spring mud and the altered sediments from both acidic and near-neutral environments. Thus, there is only minor acid-sulfate driven residual enrichment of silica at Devil's Kitchen. There is more significant acid-sulfate residual enrichment of silica at other hydrothermal sites in Lassen like Little Hot Springs Valley (e.g. McHenry et al., 2017).

54

The Paso Robles class soils are among the most altered materials found in Gusev crater because of their high SO_3 concentrations (>31 wt%) and their Fe^{3+} sulfate mineralogy (Hausrath et al., 2013). Yen et al. (2008) suggested that these altered soils were formed by the hydrothermal or fumarolic alteration of the basaltic substrate by acidic liquids or vapors. Sulfur concentrations of the most sulfur-rich altered sediments and precipitates at Devil's Kitchen were not directly measured because the sulfur concentrations of these samples were well above the rage of our XRF calibration, so we are unable to directly compare concentrations between the two sites. The altered sediments and precipitates at Devil's Kitchen undoubtedly have a high concentration of sulfur due to the abundance of sulfate minerals identified using XRD. Fe^{3+} sulfate minerals (e.g. halotrichite and jarosite) are also present around many of the hot springs at Devil's Kitchen. Qualitatively, the Paso Robles class soils and the altered sediments and precipitates at Devil' Kitchen are similar because they both have Fe^{3+} sulfate minerals abundant sulfur.

Mineral suites

Specific sulfate phases present in the sulfur-rich soils, like the Paso Robles soils, cannot be determined using the tools available to the Spirit rover (Mössbauer APXS, and Pan Cam). However, the data shows that Fe^{3+} and Mg^{2+} rich sulfates likely dominate, along with some possible Ca-sulfate phases (Yen et al., 2008). This is consistent with the high iron and magnesium content of the high-Fe basaltic substrate on Mars. At Lassen, Al^{3+}, Na^+, and Fe^{3+} sulfates are dominant with less common Ca^{2+} and K^+ sulfates because of the dacitic composition of the substrate. The Fe^{3+} sulfates at Devil's Kitchen could be the product of oxidation of pyrite at depth beneath the hydrothermal area. The sulfate phases are different on Mars and at

Lassen due to their different substrate compositions, but the same processes are at work. Specific sulfate phases associated with hydrothermal environments form depending on the cations present in the substrate rocks being altered.

Opal-A is the dominant silica phase detected near Home Plate while tridymite is dominant at Devil's Kitchen with lesser amounts of cristobalite and amorphous silica (likely Opal-A). Opal-A is less common on Earth because it undergoes diagenesis relatively quickly and changes to quartz (e.g. Lynne et al., 2006). The cooler, drier environment on Mars allows Opal-A to be preserved at the surface longer while on Earth it more quickly undergoes diagenesis. Even though it is much less common than it is on Mars, amorphous silica is still present at Devil's Kitchen. Three samples from a site #1 (a near-neutral hot spring, pH 5) had amorphous silica precipitates with geochemical patterns consistent with direct precipitation. One sample (L-17-DK-25) from an acidic site (pH of 3.2) had amorphous silica as well, but showed geochemical patterns consistent with acid-sulfate leaching rather than precipitation from a silica-rich fluid. This demonstrates how amorphous silica can be produced by direct precipitation from a silica-rich fluid and by acid-sulfate leaching within the same system on a very small spatial scale. If the silica-rich nodular deposits at Home Plate were formed by near-neutral silica sinter precipitation, Devil's Kitchen could be a good terrestrial analog demonstrating that there can be both near-neutral silica sinter precipitation (L-17-DK-04) and minor acid-sulfate leaching (L-16-DK-11, L-17-DK-18, 24, and 25) within the same hydrothermal system within a few meters of each other. Thus the presence of sulfate-rich soil at Home Plate, which indicates acid-sulfate leaching, doesn't preclude the presence of near-neutral silica sinter producing environments within the same system at the same time.

<u>**Habitability**</u>

On Earth, near-neutral and acidic hydrothermal environments are habitable, but the biomass and diversity of acidic environments is much lower than in near-neutral environments (e.g. Goorissen et al., 2003). The SEM analysis in this study shows that at Devil's Kitchen, both the acidic and near-neutral hot springs represent habitable environments. Biosignatures in both of these environments had a high preservation potential due to the rapid precipitation of silica on the surfaces on which these organisms were living. The silica-rich nodular outcrops near Home Plate suggest a near-neutral hydrothermal origin (Ruff et al., 2011). The large amounts of silica sinter precipitating near Home Plate means that if there were any biosignatures present, they would have a very high preservation potential. Even if there were no organisms at any time on Mars, the proposed hydrothermal deposits at Home Plate could represent a once habitable environment.

<u>**Conclusions**</u>

- Devil's Kitchen yields a diverse suite of minerals including primary igneous phases, clay minerals, sulfates, and silica phases. The primary igneous phases reflect the dacitic composition of the substrate and are dominated by plagioclase and tridymite with some potassium feldspar. The tridymite likely reflects an earlier, higher temperature hydrothermal system because the current system doesn't have high enough temperatures to form tridymite. Tridymite forms at 870-1470 °C, which is well above the temperatures in the current hydrothermal system. Amorphous silica precipitate coatings were observed on rock samples collected from a near-neutral hot spring (pH 5) at site #1. The dominant clay

57

phase present is kaolinite which reflects the abundant aluminum in the system. Sulfate phases are dominated by Al^{3+}, Fe^{3+}, and Na^+ phases with lesser amounts of Ca^{2+} and K^+ phases. Jarosite was observed in three samples, all of which were from more acidic, oxidizing hot springs. Jarosite can be used as an indicator of acidic, oxidizing conditions at the time of deposition.

- Geochemical analyses of hot spring mud samples show similar geochemical patterns in acidic and near-neutral environments. Both environments showed depletion of more mobile cations (Mn^{2+}, Mg^{2+}, Ca^{2+}, and Na^+) compared to the substrate composition. This is consistent with minor acid-sulfate leaching of altered rocks with a high water-rock ratio. The mud samples show uniform enrichment in titanium which is less mobile. Silica and aluminum content of hot spring muds show both slight enrichment and slight depletion depending on the sample. Enrichment in titanium with variable enrichment and depletion of silica shows a decoupling of silica and titanium concentrations indicating that silica is being removed from the mud while titanium is left behind.

- Geochemical analyses of the altered sediment samples show more variation between acidic and near-neutral environments. Both acidic and near-neutral sediments were generally depleted in more mobile cations. Altered sediments from the acidic environments are uniformly depleted in Al_2O_3 while some altered sediments from the near-neutral environments show enrichment due to their kaolinite component. Where amorphous silica was present in near-neutral environments (e.g. L-17-DK-04) silica is enriched and titanium is depleted,

58

consistent with silica precipitation rather than residual enrichment through acid-sulfate leaching. Where amorphous silica is present in acidic environments (e.g. L-17-DK-25) silica and titanium are both enriched, consistent with residual enrichment through acid-sulfate leaching.

- Water chemistry shows that the acidity of the system is controlled by the concentration of sulfate dissolved in the water, with high sulfate concentrations driving the pH of the water down. Calcium and sodium are the most abundant dissolved cations with lesser amounts of potassium and magnesium. Consistent with the dissolution of the plagioclase-rich dacitic substrate. The more acidic water samples tend to have a higher concentration of dissolved cations. There is also a strong positive correlation between sulfate concentration and dissolved iron, which could be caused by the oxidation of pyrite at depth beneath the hot springs.

- SEM analysis shows that both the acidic and near-neutral hydrothermal environments at Devil's Kitchen represent habitable environments. Abundant biological structures are present in the samples collected from the hot springs including rod-shaped microbes, algae cells, diatoms, phytoplankton, pollen grains, and biofilms. Amorphous silica coatings were observed on many of the biological structures. This demonstrates the high preservation potential of silica precipitating hydrothermal environments.

- The Devil's Kitchen hydrothermal system could be a terrestrial analogue for understanding the chemical conditions of the hydrothermal fluids associated

with the proposed Home Plate hydrothermal system on Mars. The Devil's Kitchen system demonstrates that minor acid-sulfate leaching and precipitation of amorphous silica from near-neutral hydrothermal fluids can occur within the same system within a few meters of each other. The Home Plate hydrothermal system could have followed a similar pattern with acid-sulfate leaching forming the Paso Robles class soils and near-neutral silica sinter precipitating hot springs forming the silica-rich nodular outcrops. While silica enrichment in the silica-rich soils at Home Plate are considerably higher than at Devil's Kitchen, this site demonstrates that the presence of acid-sulfate leaching doesn't preclude near-neutral silica sinter precipitation from the same system on a small spatial scale.

The goal of this research was to help constrain hydrothermal alteration patterns associated with acidic and near-neutral hot springs so that comparisons could be made to better our understanding of potential hydrothermal deposits on Mars. A better understanding of the specific mineral phases present at Home Plate and a more detailed analysis of the silica-rich nodular outcrops will refine our understanding of the environmental conditions associated with these deposits and their potential for habitability.

References

Anrorsson, S., Bjarnason, J.O., Giroud, N., Gunnarson, I., and Stefasnsson, A., (2007). Fluid-fluid interactions in geothermal systems, Rev. Mineralogy and Geochemistry. 65, 259-312.

Arvidson, R.E. et al., (2008). Spirit Mars Rover mission to the Columbia Hills, Gusev Crater: Mission overview and selected results from the Cumberland Ridge to Home Plate. Journal of Geophysical Research. 113

Byers, H., McHenry, L.J., and Grundl, T.J., (2016). Forty-nine major and trace element concentrations measured in Soil Reference Materials NIST SRM 2586, 2587, 2709a, 2710a and 2711a using ICP-MS and Wavelength Dispersive-XRF, Geostandards and Geoanalytical Research, 40, 433-445.

Cady S.L., Farmer J.D., (1996). Evolution of Hydrothermal Ecosystems on Earth (and Mars?). G. Bock, J. Goode, Eds. (J. Wiley and Sons, Chichester, UK, 1996), pp. 150-173.

Clynne M.A., Janik, C.J., and Muffler, L.J.P., (2003). "Hot water" in Lassen Volcanic National Park – Fumaroles, steaming ground, and boiling mudpots. U.S. Geologic Survey Face Sheet 101-02.

Crowley, J.C., John, D.A., Muffler, L.J.P., and Clynne, M.A., (2004). Hydrothermal mineral zoning within an eroded stratocone: remote sensing spectral analysis of Brokeoff Volcano, California. In: King P.L. Ramsey, M.S., Swayze, G.A. (Eds.), Infrared Spectroscopy in Geochemistry, Exploration Geochemistry, and Remote Sensing. Mineralogical Association of Canada Short Course, vol. 33. Ontario, London, pp. 215-226.

Goorissen, H.P. Boschker, H.T., Stams, A.J, and Hansen, T.A., (2003). Isolation of thermophilic Desulfotomaculum strains with methanol and sulfite from solfataric mud pools, and characterization of Desulfotomaculum solfataricum sp. Nov. International Journal of Systematic and Evolutionary Microbiology, 53, 1223-1229

Hausrath, E.M., Golden, D.C., Morris, R.V., Agresti, D.G., and Ming, W., (2013). Acid sulfate alteration of fluorapatite, basaltic glass and olivine by hydrothermal vapors and fluids: Implications for fumarolic activity and secondary phosphate phases in sulfate-rich Paso Robles soil at Gusev Crater, Mars. Journal of Geophysical Research: Planets, Vol. 118, 1-13

Hynek, B. M. Beach, M., and Hoke, M.R.T. (2010). Updated global map of Martian valley networks and implications for climate and hydrogeologic processes. Journal of Geophysical Research, 115, E09008.

Hynek, B. M., McCollom, T.M., Marcucci, E.C., Brugman, K., and Rogers, K.L., (2013). Assessment of environmental controls on acid-sulfate alteration at active volcanoes in Nicaragua: Applications to relic hydrothermal systems on Mars. Journal of Geophysical Research: Planets. Vol. 118, 2083-2104.

Ion Chromatography in Water Analysis, Oleg Shpigun, Yuir A. Zolotov, Wiley (New York 1988).

Ingebritsen. S.E., Bergfield. D., Clor. L.E. and Evans. W.C. (2016) The Lassen hydrothermal system. American Mineralogist. 101. 343-353.

James S. Fritz, Douglas T. Gjerde, Christel Pohlandt, Huthig Verlag (Heidelberg1982) Ion Chormatography, Hamish Small, Plenum (New York 1989).

Janik, C.J., and McLaren, M.K., (2010). Seismicity and fluid geochemistry at Lassen Volcanic National Park, California: Evidence for two circulation cells in the hydrothermal system. Journal of Volcanology and Geothermal Research 189: 257-277.

John, D.A., Rytuba, J.J., Breit, G.N., Clynne, M.A., and Muffler, L.J.P. (2005) Hydrothermal alteration in Maidu Volcano: A shallow fossil acid-sulfate magmatic-hydrothermal system in the Lassen Peak area. California in Rhoden H.N., Steiger, R.C., and Vikre, P.G., eds., Geologic Society of Nevada Symposium 2005: Window to the World, Reno, Nevada. May 2005, 295-313

Krebs, J.E., Vaishampayan, P., Probst, A.J., Tom, L.M., Marteinsson, V.T., Andersen, G.L., and Venkateswaran, K., (2014). Microbial Community Structures of Novel Icelandic Hot Spring Systems Revealed by PhyloChip G3 Analysis. Astrobiology, 14, 299-240.

Kuniaki Kihara, Matsumoto T., and Imamura M. (1986). "Structural change of orthorhombic-I tridymite with temperature: A study based on second-order thermal-vibrational parameters". Zeitschrift für Kristallographie. 177: 27–38.

Lynne B.Y., Campbell, K.A., Perry, R.S., Browne, P.R.L., and Moore, J.N., (2006). Acceleration of sinter diagenesis in an active fumarole, Taupo volcanic zone, New Zealand. Geology, Vol. 24, 749-752.

Lynne B.Y., Campbell, K.A., James, B.J., Browne, P.R.L., and Moore J.N., (2007). Tracking Crystallininty in Siliceous Hot-Spring Deposits. Journal of Science. Vol. 307, March, 2007, P. 612-641

Markusson, S.H., and Stefansson, A., (2011). Geothermal surface alteration of basalts, Krysuvik Iceland – Alteration mineralogy, water chemistry and the effects of acid supply on the alteration process. Journal of Volcanology and Geothermal Research, 206, 46-59.

Martin, W., Baross, J., Kelley,. D., and Russell, M.J., (2008). Hydrothermal vents and the origin of life. Nat. Rev. 6, 805-814.

McHenry, L.J., (2009). Element mobility during zeolitic and argillic alteration of volcanic ash in a closed-basin lacustrine environment: Case study Olduvai Gorge, Tanzania. Chemical Geology 265, 540-552.

McHenry, L.J., Carson, G.L., Dixon, D.T., and Vickery, C.L., (2017). Secondary minerals associated with Lassen fumaroles and hot springs: Implications for martian hydrothermal deposits. American Mineralogist, Vol. 102, 1418-1434

McHenry, L. J., Gerard, T.L., and Walters, G.L., (2013). Lassen volcanic fumaroles and hot springs: analogue for Mars. Journal of Geophysical Research. 2013.

McHenry, L. J., Vincent, C., and Schroder, C., (2011). Jarosite in a Pleistocene East African saline-alkaline paleolacustrine deposit: Implications for Mars aqueous geochemistry. Journal of Geophysical Research, Vol. 116. 2011

McSween, H.Y., Ruff, S.W., Morris, R.V., Bell, J.F. III, Herkenhoff, K., Gellert, R., Stockstill, K.R., Tornabene, L.L., Squyres, S.W., Crisp, J.A., Chirstensen, P.R., McCory, T.J., Mittlefheldt, D.W., and Schmidt, M. (2006). Alkaline volcanic rocks from the Columbia Hills, Gusev Crater, Mars. Journal of Geophysical Research, 101, E09S91.

McSween, H.Y.J., Taylor, G.J., and Wyatt, M.B., (2009). Elemental composition of the Martian Crust. Science 324: 736-739.

Michalski, J.R. et al., (2008). Journal of Geophysical Research. 108, 8064 (2003)

Ming, D.W., et al., (2008). Geochemical properties of rocks and soils in Gusev Crater, Mars: Results of the Alpha Particle X-Ray Spectrometer from Cumberland Ridge to Home Plate. Journal of Geophysical Research, Vol. 113, EL2S39.

Morris, R.V., Vaniman, D.T., Blake, D.F., Gellert, R., Chipera, S.J., Rampe, E.B., Ming, D.W., Morrison. S.M., Downs, R.T., Treiman, A.H., and others. (2016). Silicic volcanism on Mars evidenced by tridymite in high SiO_2 sedimentary rocks at Gale Crater. Proceedings of the National Academy of Sciences, 113, 7071-7076.

Muffler, L.J.P., Nehring, N.L., Treusdell, A.H., Janik, C.J., Clynne, M.A., and Thompson, J.M., (1982). The Lassen geothermal system: U.S. Geological Survey Open-File Report 82-926, 8 p. Also published in the Proceedings of the Pacific Geothermal Conference, Auckland, New Zealand November 1982.

Ruff, S.W. Farmer, J.D., Calvin, W.M., Herkehoff, K.E., Johnson, J.R., Morris, R.V., Rive, M.S., Arvidson, R.E., Bell, J.F. III, Christensen, P.R., and Squyres, S.W., (2011). Characteristics, distribution, origin, and significance of opaline silica observed by the Spirit Rover in Guesev crater. Mars. Journal of Geophysical Research 116: E00F23.

Ruff, S. W., and Farmer, J. D. (2016). Silica deposits on Mars with features resembling hot spring biosignatures at El Tatio in Chile. Nature Communications, 7, 13554.

Schmidt, M.E., Ruff, S.W., McCoy, T.J., Farrand, W.H., Johnson, J.R., Gellert, R., Ming, D.W., Morris, R.V., Cabrol, N.A., Lewis, K.W., and Schroder, C., (2008). Hydrothermal origin of halogens at Home Plate, Gusev Crater. JGR 113: E06S12.

Squyres et al., (2004). The Spirit Rover's Athena science investigation at Gusev Crater, Mars. Science 305, 794–9.

Squyres et al., (2007). Pyroclastic Activity at Home Plate in Gusev Crater, Mars. Science (80-.). 316, 738–742.

Sqyures et al., (2008). Detection of silica-rich deposits on Mars, Science, 320, 1063-1067

Standard Methods for the Examination of Water and Wastewater, 17th ed. (1989). pages 3-1 to 3-23 (introduction), page 3-85 (Calcium), page 3-112 (Magnesium), page 3-125 (Potassium), page 3-145 (Sodium), [16th ed., (1985) Sections 301 (Introduction), pp. 143-4; 303 and 303A (Calcium and Magnesium), pp. 151-60; 322 and 322A (Potassium), pp. 236-7; and 325 and 325A (Sodium), pp. 245-9.]

Standard Methods for Examination of Water and Wastewater, 17th ed. (1989). Section 4110 "Determination of Anions by Ion Chromatography" pp. 4-2 to 4-6. [16th ed. (1985) Section 429 "Determination of Anions by Ion Chromatography" pp. 483-8).

Staudt C, Horn H, and Hempel DC, Neu TR (2004). "Volumetric measurements of bacterial cells and extracellular polymeric substance glycoconjugates in biofilms". *Biotechnol. Bioeng*. 88 (5): 585–92.

Winter, J. D., & Winter, J. D. (2010). Principles of igneous and metamorphic petrology. New York: Prentice Hall.

Yen. A.S., Morris, R.V., Clark, B.C., Gellert, R., Knudson, A.T., Squyres, S., Mittlefhldt, D.W., Ming, D.W., Arvidson, R., McCoy, T., and others. (2008). Hydrothermal Processes at Gusev Crater: An evaluation of Paso Robles class soils. Journal of Geophysical Research 113: E06S10
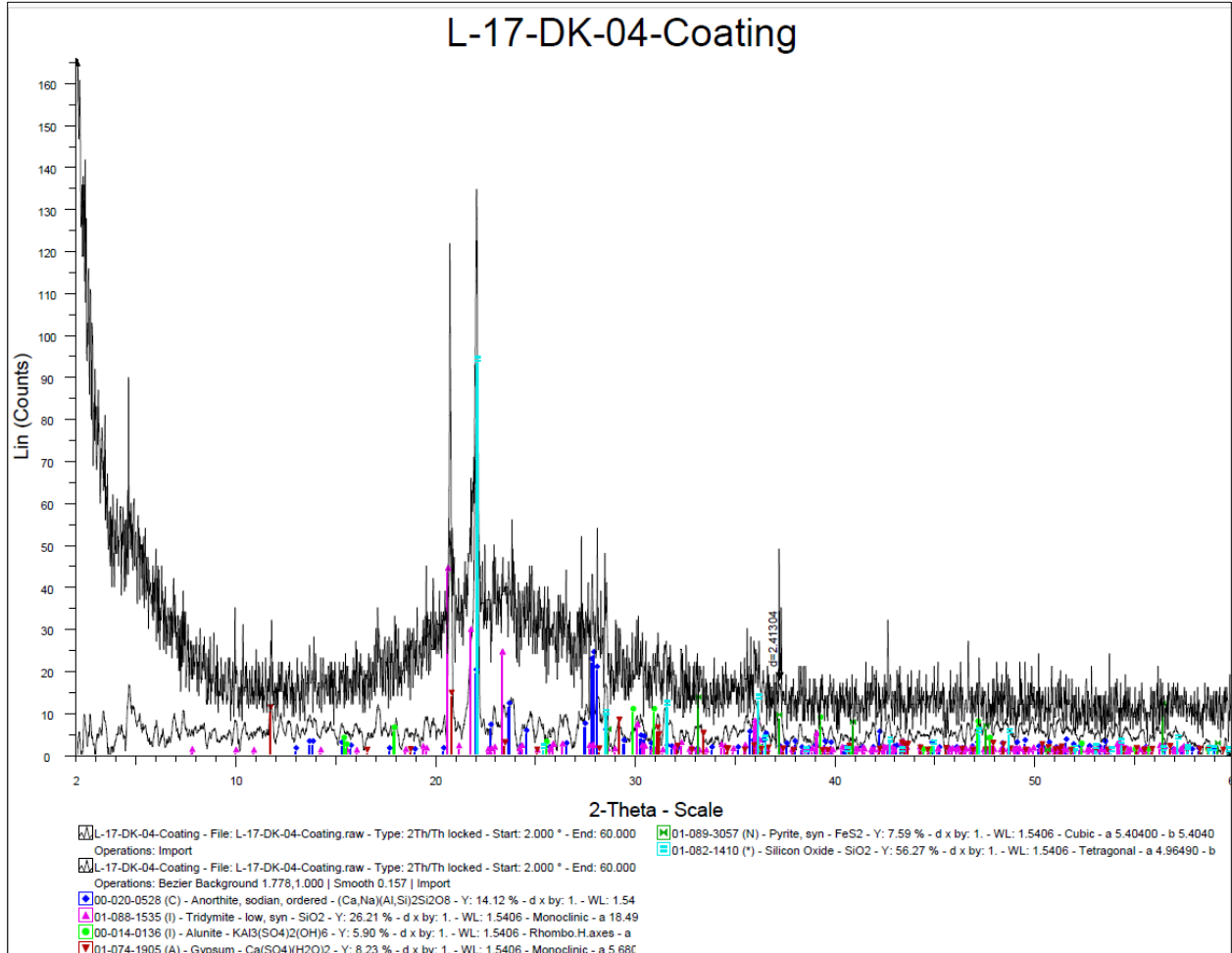
Appendix

Figure 34: XRD pattern for L-17-DK-04 (coating) showing an amorphous silica hump with other crystalline phases present. The top pattern shows the unaltered XRD scan and the lower pattern shows the same scan with background subtracted and smoothed.
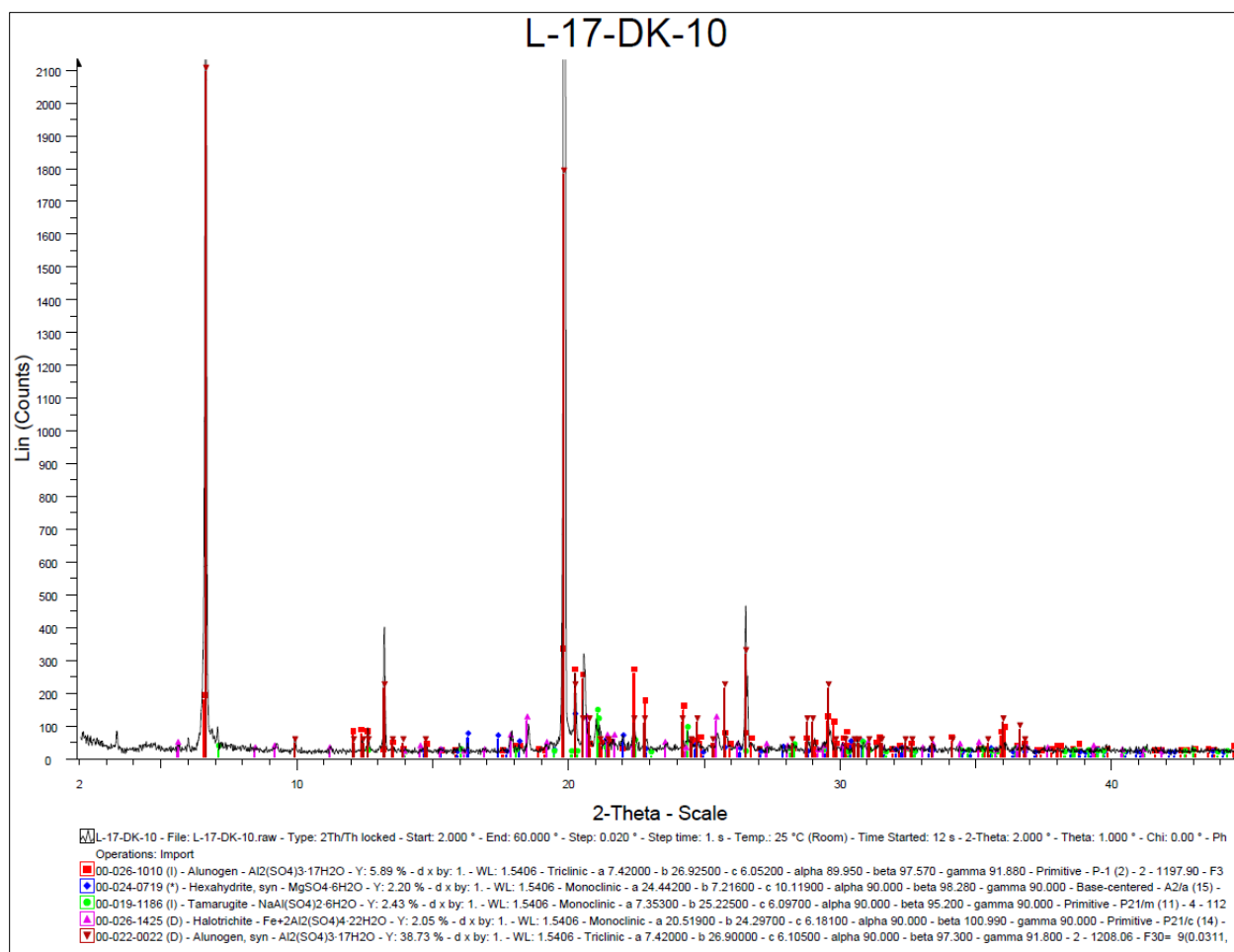
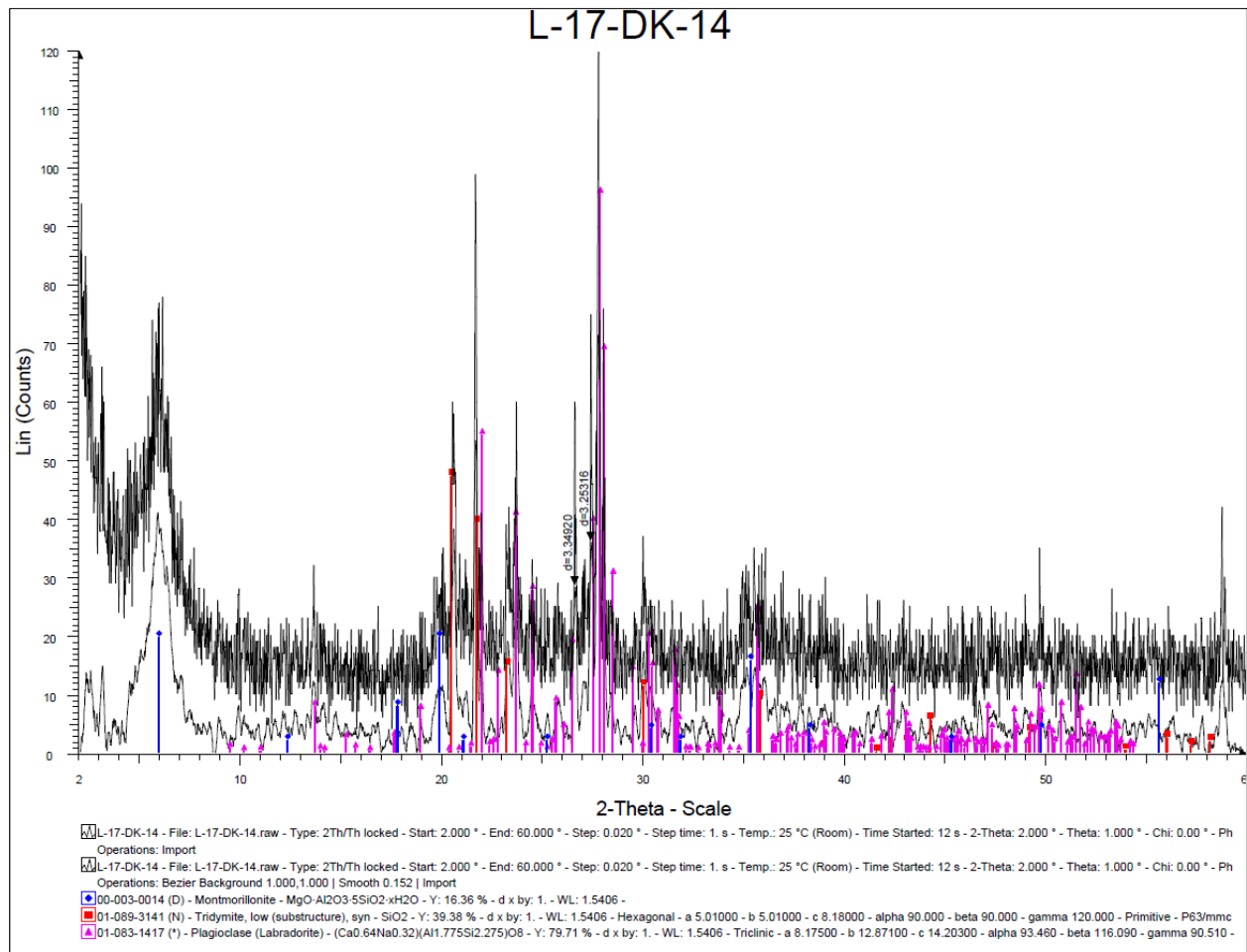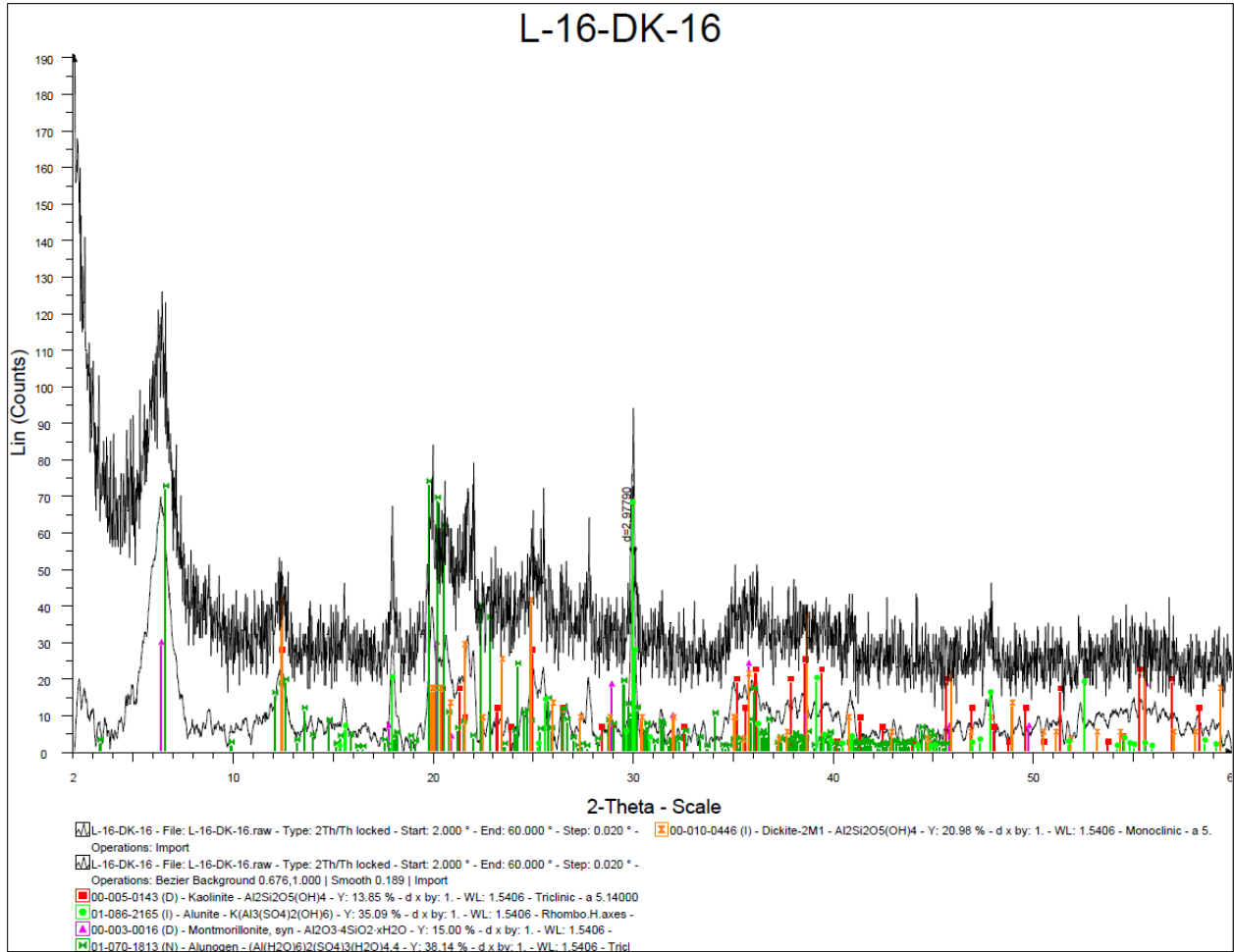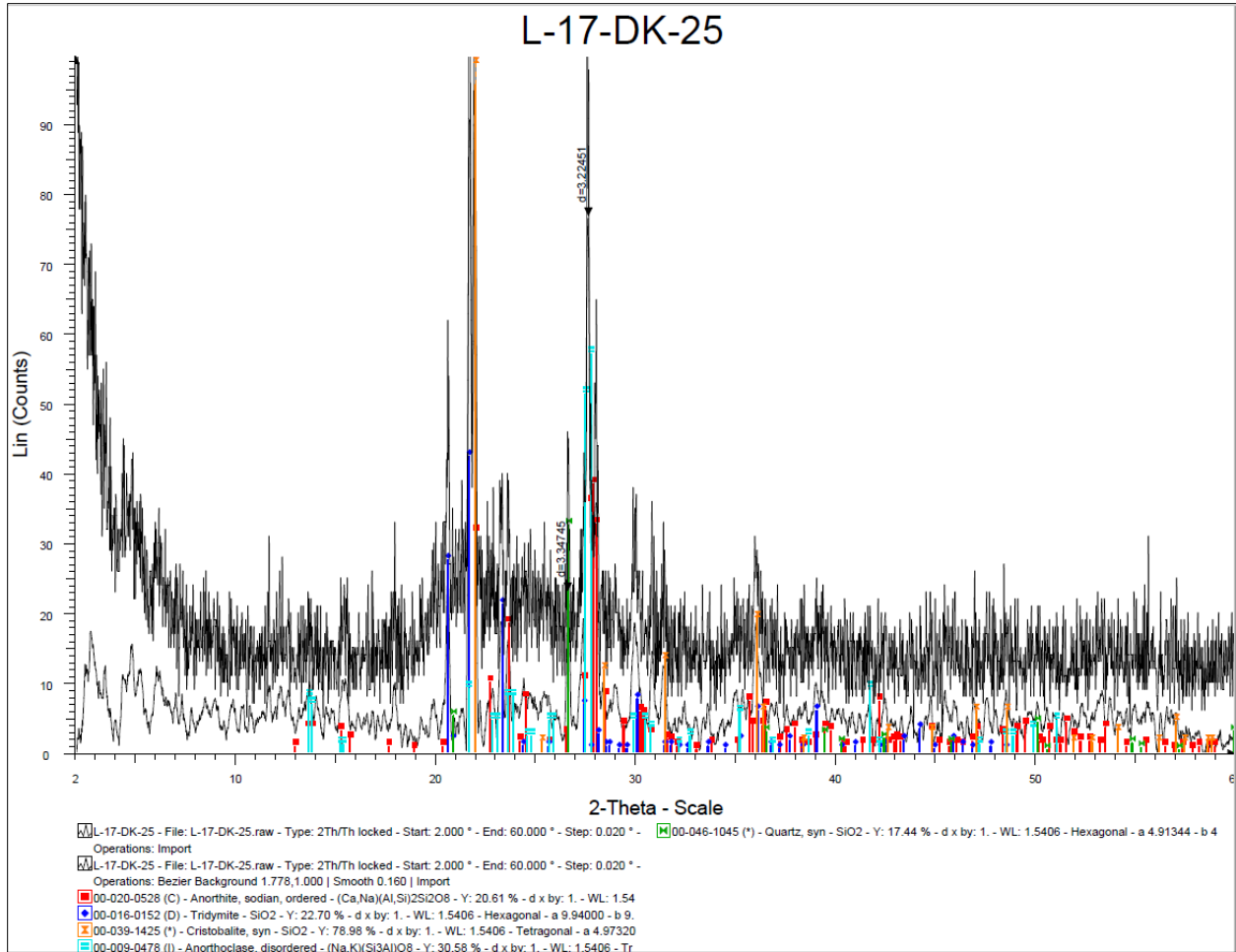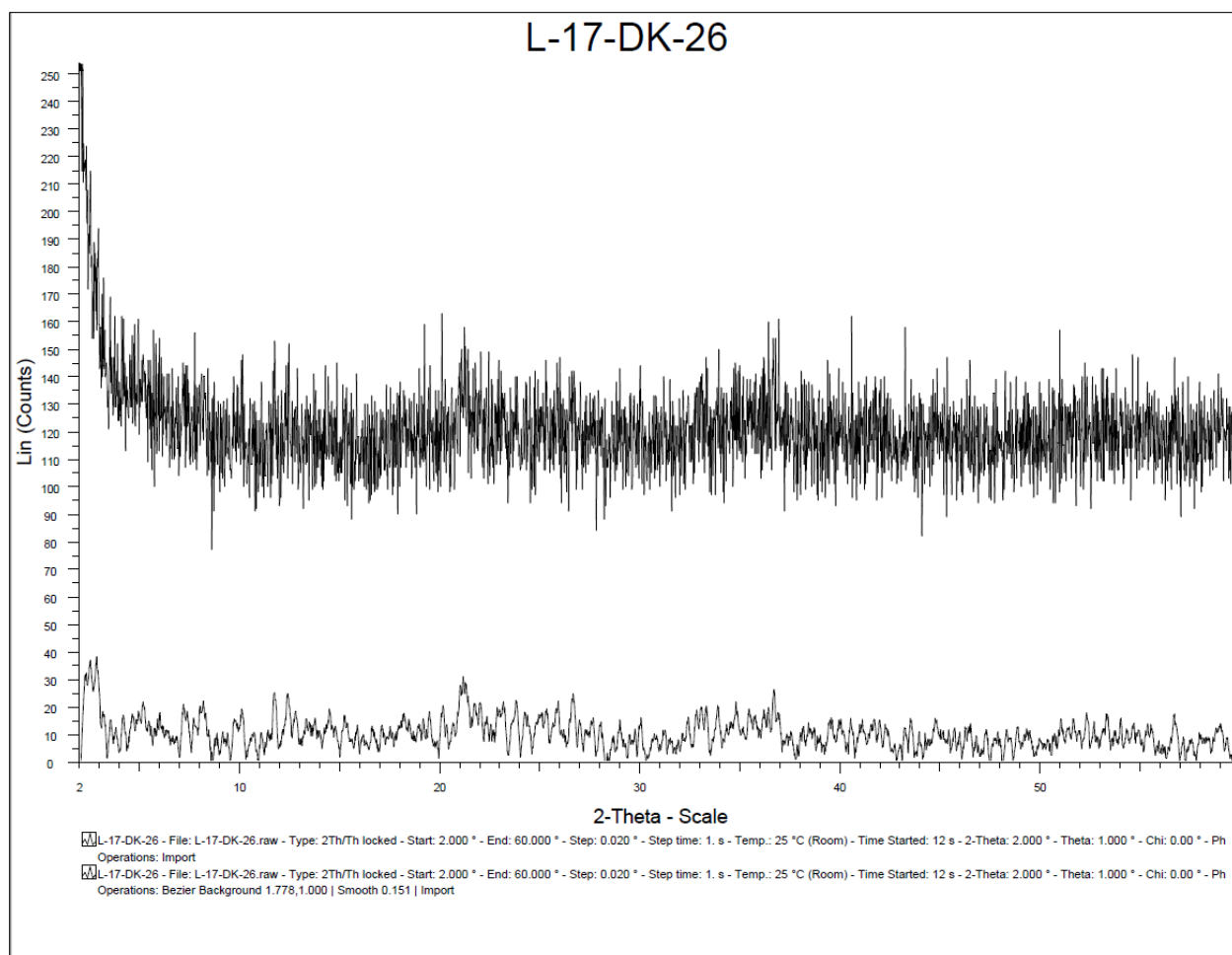**Figure 35: XRD pattern for L-17-DK-10 showing a representative precipitate sample.**

Figure 36: XRD pattern for L-17-DK-14 showing a representative montmorillonite clay pattern with other primary phases like plagioclase and tridymite. The top pattern shows the unaltered XRD scan and the lower pattern shows the same scan with background subtracted and smoothed.

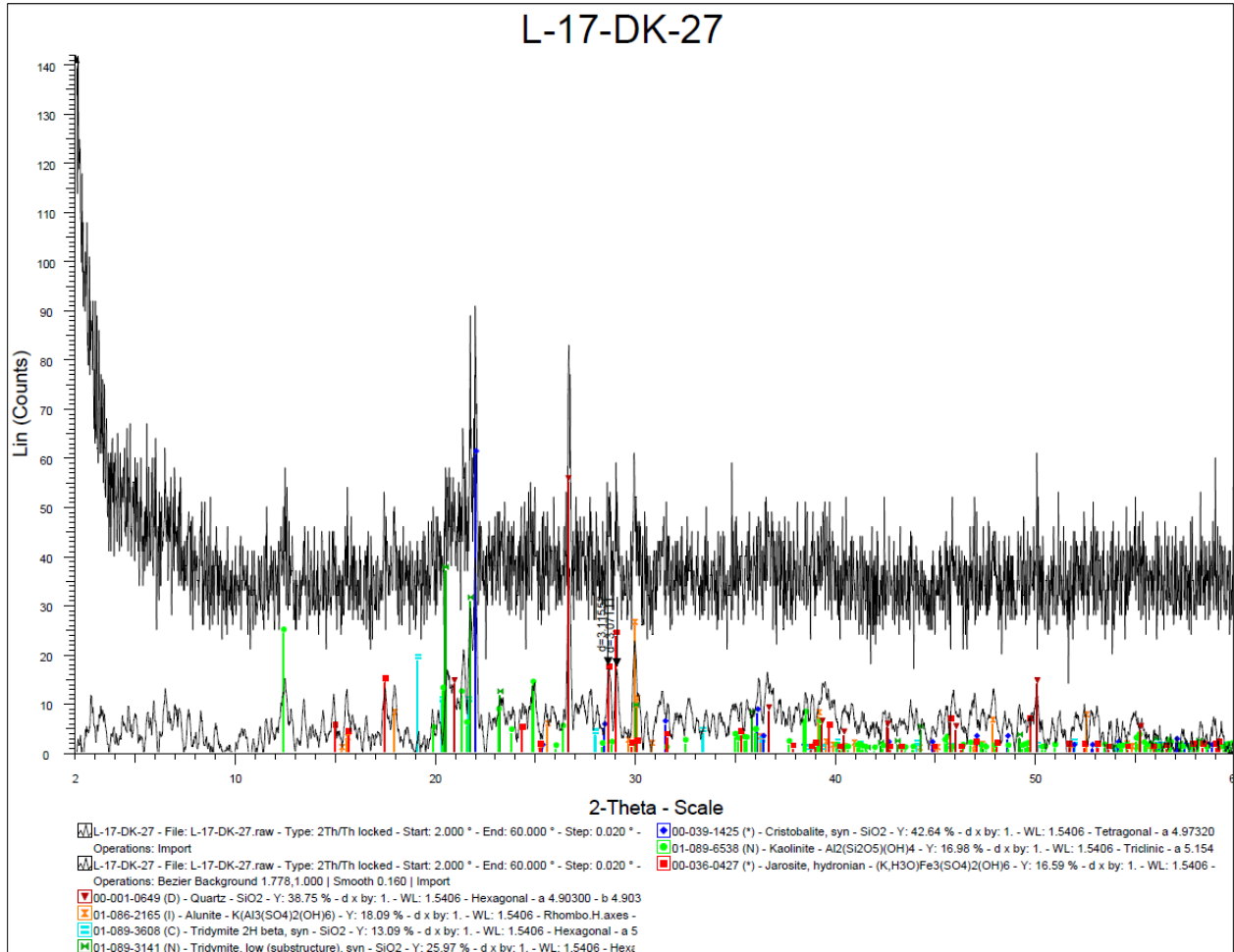**Figure 37: XRD pattern for L-17-DK-16 showing a representative kaolinite and montmorillonite pattern with some precipitates incorporated into it. The top pattern shows the unaltered XRD scan and the lower pattern shows the same scan with background subtracted and smoothed.**

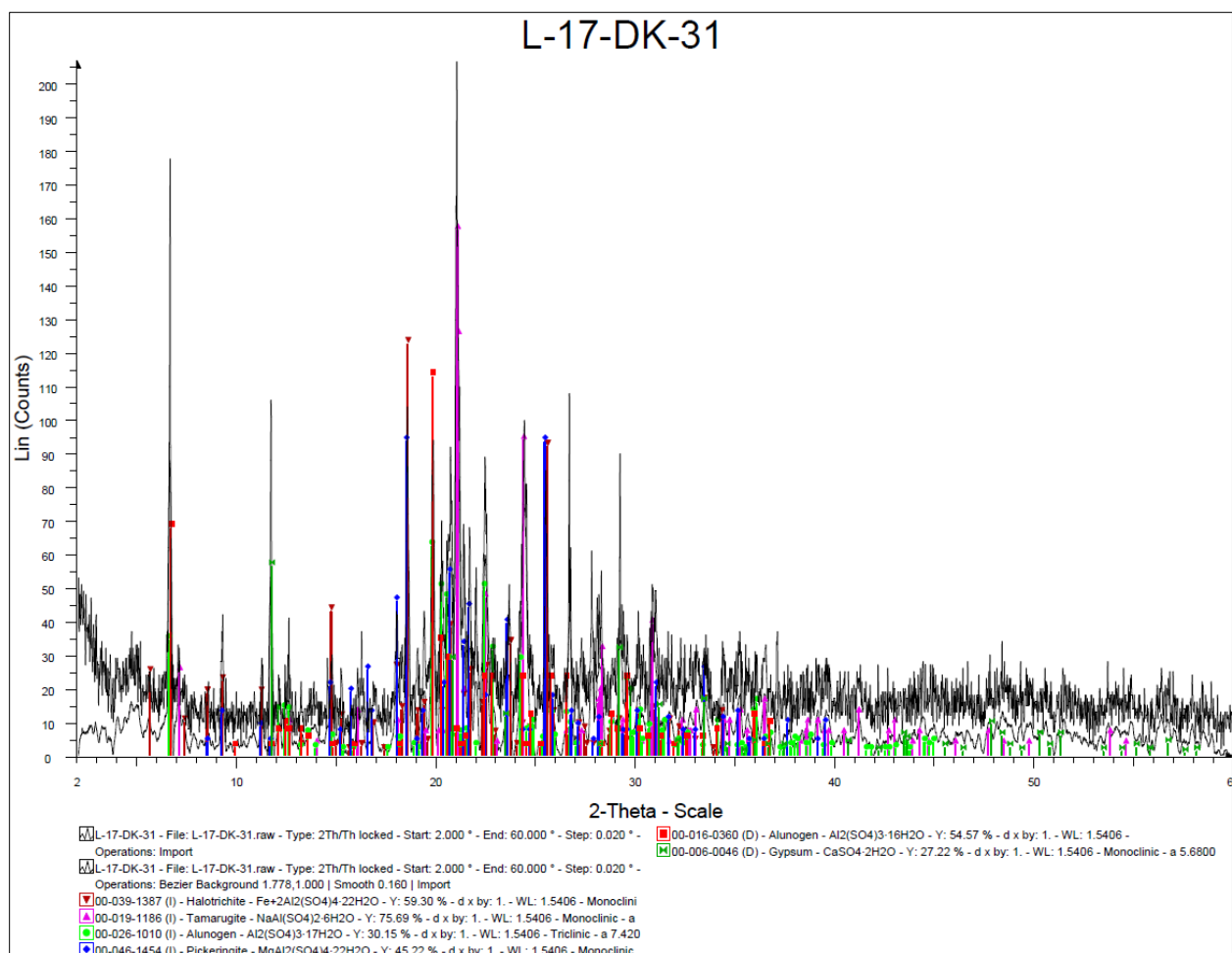**Figure 38: XRD pattern for L-17-DK-25 showing an amorphous silica hump with other silica phases and igneous substrate phases. The top pattern shows the unaltered XRD scan and the lower pattern shows the same scan with background subtracted and smoothed.**

Figure 39: XRD pattern for L-17-DK-26 showing a sample that did not show any significant diffraction, and exhibited particularly high background (likely because of Fe fluorescence). The top pattern shows the unaltered XRD scan and the lower pattern shows the same scan with background subtracted and smoothed.

**Figure 40: XRD pattern for L-17-DK-27 showing one of the samples analyzed using SEM. Representative pattern showing an altered sediment with silica minerals mixed with iron-rich precipitates like jarosite. The top pattern shows the unaltered XRD scan and the lower pattern shows the same scan with background subtracted and smoothed.**

Figure 41: XRD pattern for L-17-DK-31 showing a representative precipitate sample containing halotrichite/pickeringite, tamarugite, alunogen, and gypsum. The top pattern shows the unaltered XRD scan and the lower pattern shows the same scan with background subtracted and smoothed.
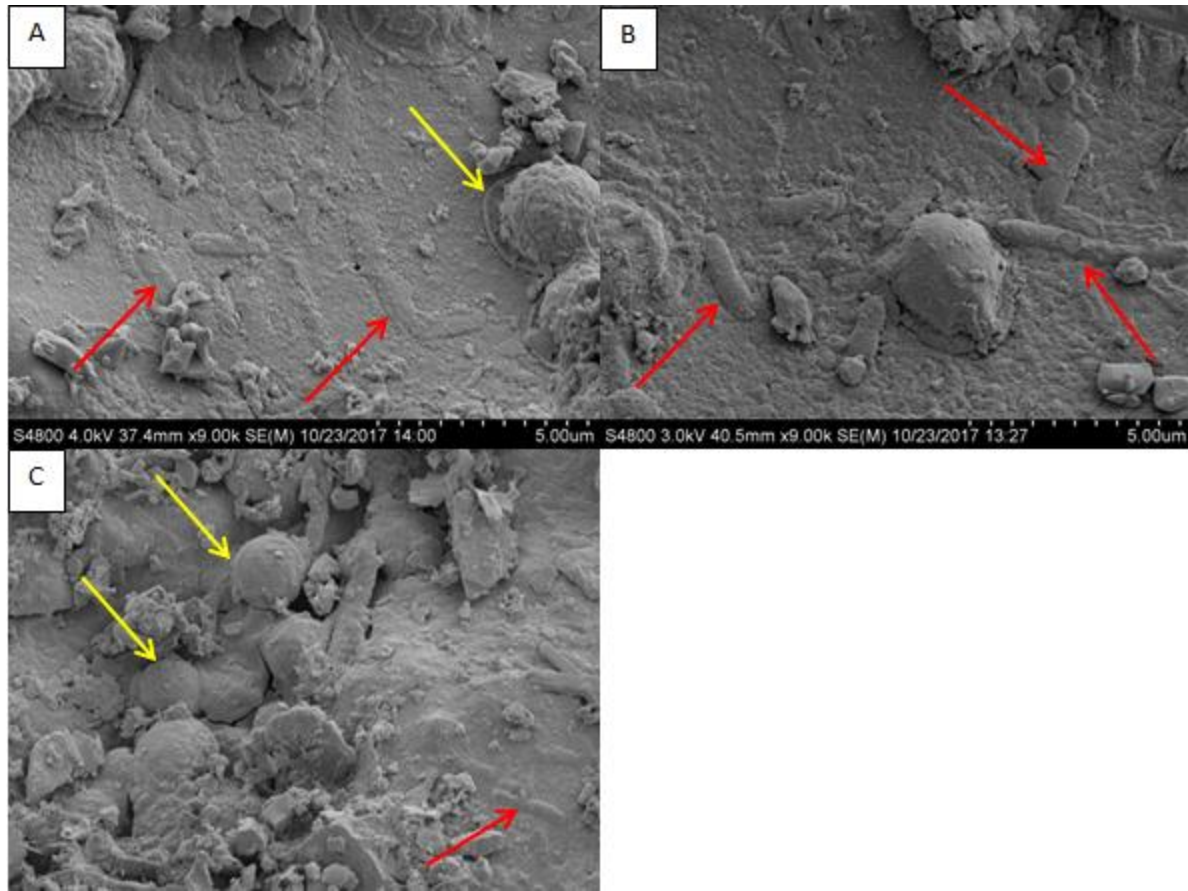
Figure 42: A-C from sample L-17-DK-04: (A) The red arrows show rod-shaped microbes in close association with algae cells. The rod-shaped microbes look very flat and are being incorporated into the substrate. The yellow arrow shows a spherical algae cell with a distinct cell wall and intercellular material. (B) The red arrows show more distinct rod-shaped microbes covered in tiny globules of amorphous silica. The microbes are again found in close association with algae cells. (C) The yellow arrows show spherical algae cells covered in a coating of amorphous silica. The red arrow shows rod-shaped microbes almost completely covered in amorphous silica.
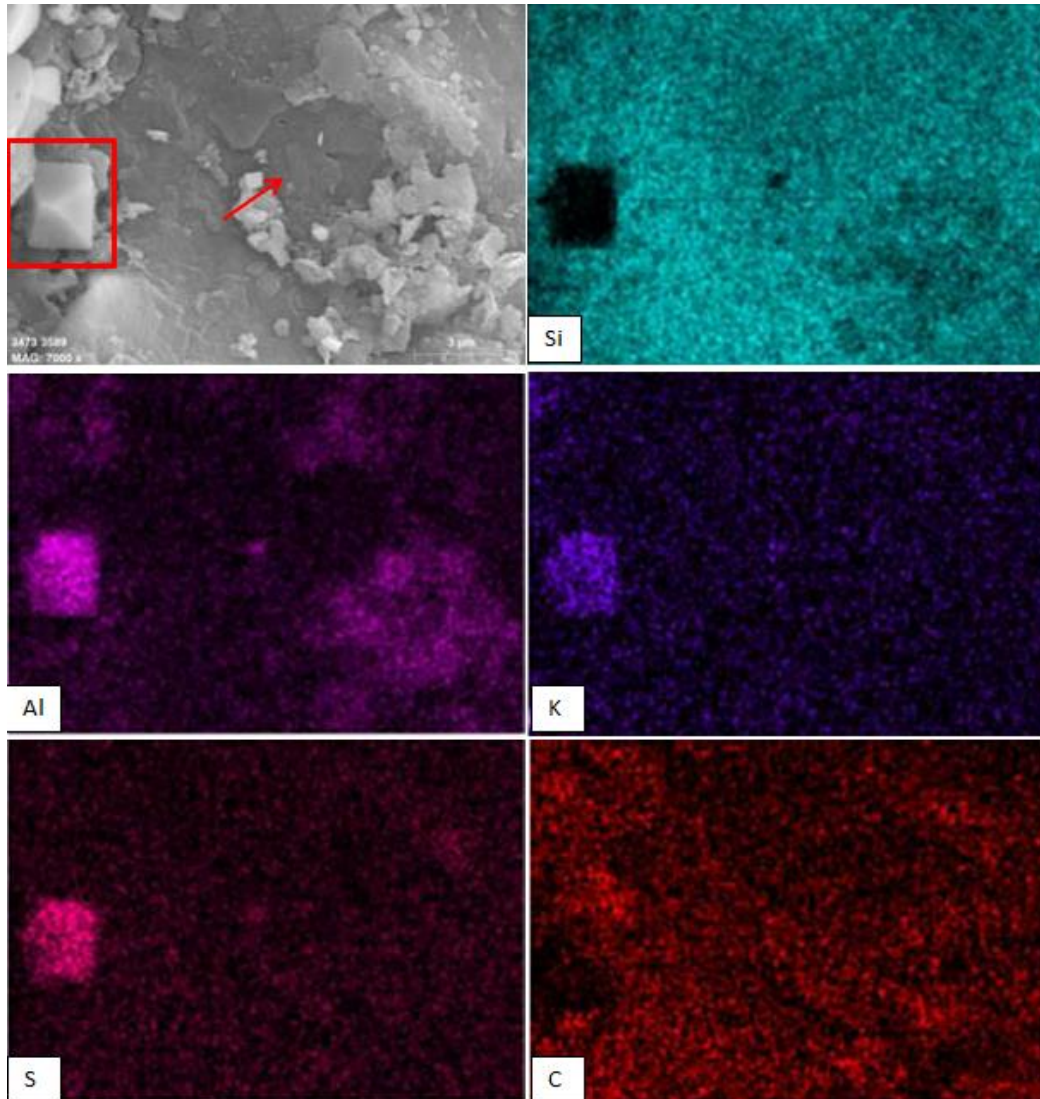
Figure 43: EDS elemental maps from sample L-17-DK-04 of an alunite crystal (in the red box) and a rod shaped microbe (at the end of the red arrow). The octahedral crystal contains no silica, and is rich in aluminum, potassium, and sulfur. This is consistent with alunite ($KAl_3(SO_4)_2(OH)_6$). The rod-shaped microbe does not stand out against the silicon rich background, indicating that is the same composition as the substrate.
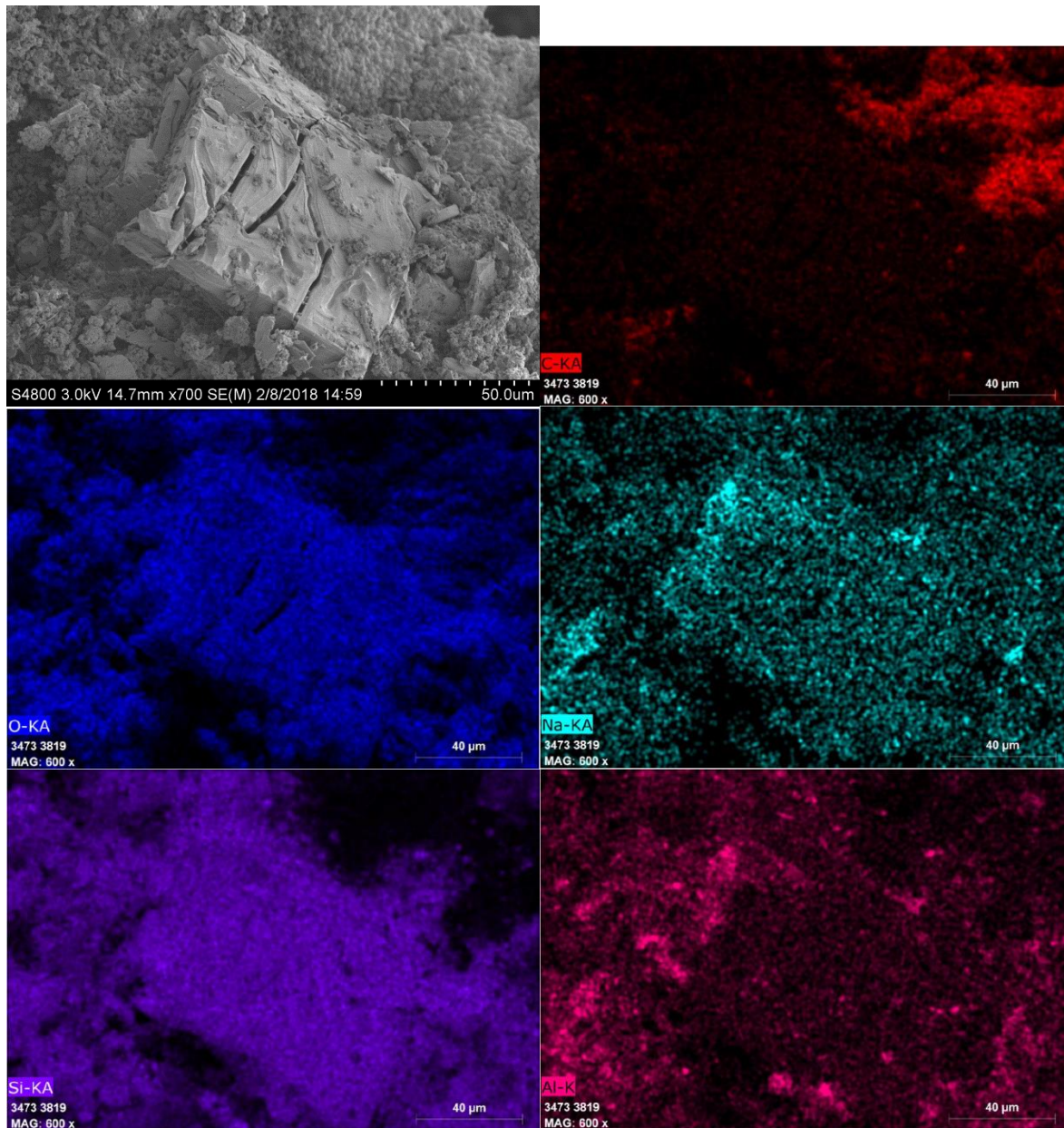
Figure 44: EDS elemental maps of sample L-17-DK-27 of a large crystal showing dissolution. The crystal is somewhat rectangular in shape and has large troughs and furrows. The crystal is rich in silicon and oxygen with minor sodium concentrations. The crystal lacks carbon and shows no elevated concentrations of aluminum.
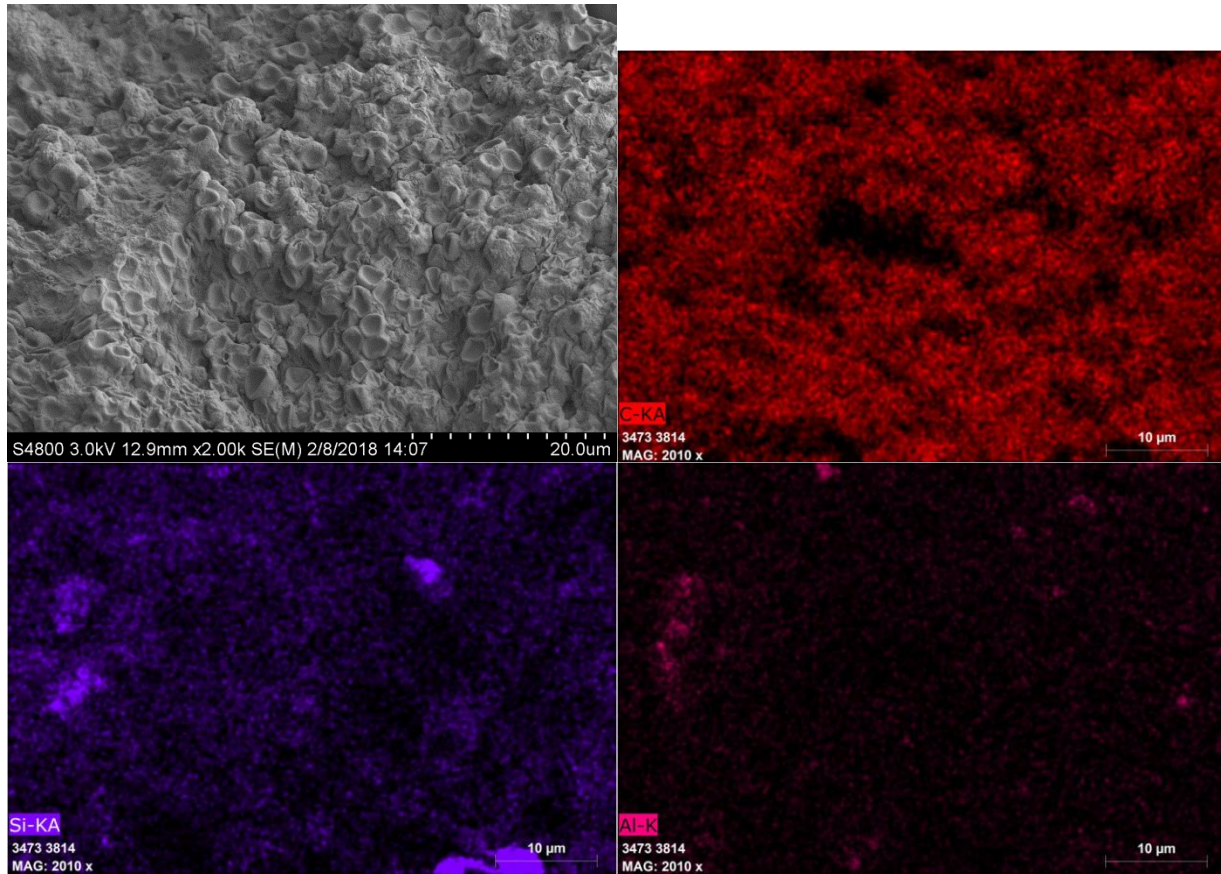
Figure 45: EDS elemental maps of sample L-17-DK-27 of biconcave algae cells. The EDS analysis shows that the entire region around the algae cells is carbon rich. The algae cells are relatively silicon poor while the regions between the algae cells are more silicon rich. The entire region is aluminum poor.
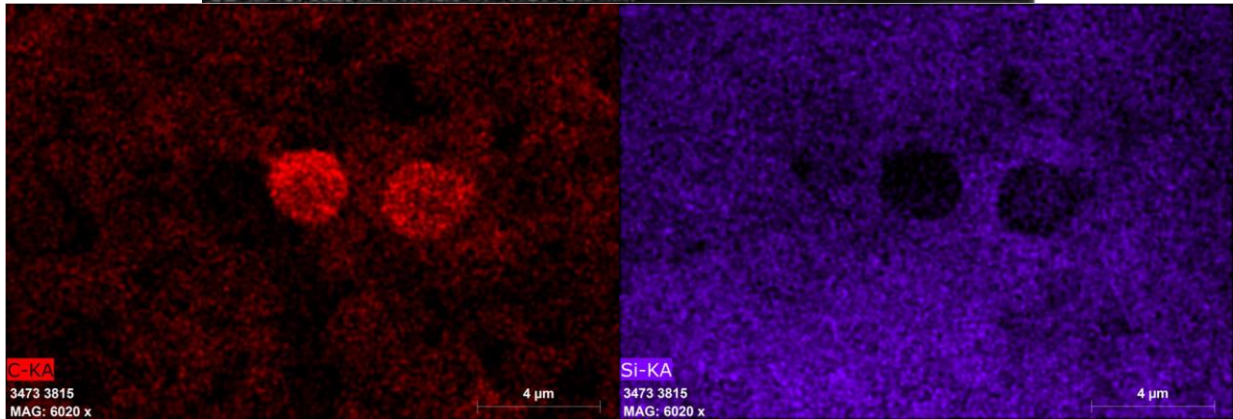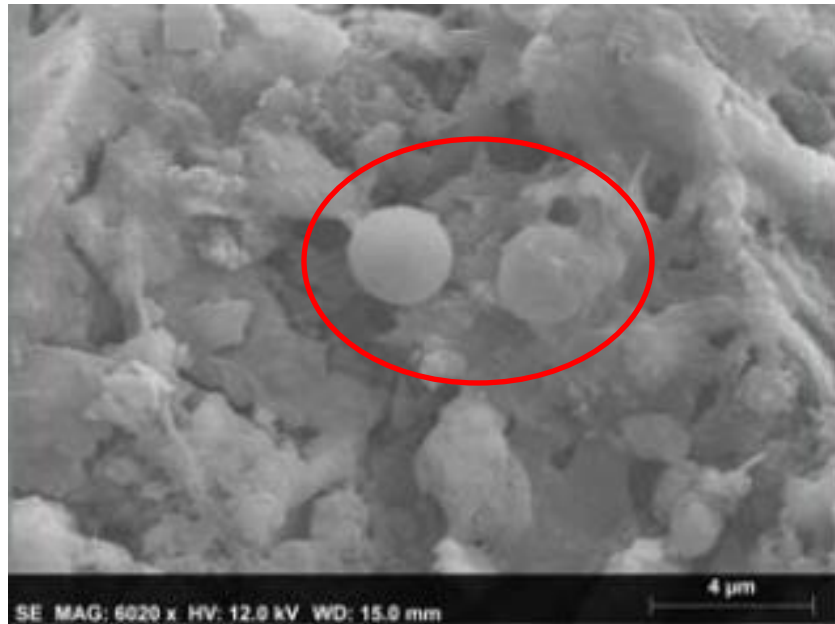
Figure 46: EDS elemental maps of sample L-17-DK-27 of two spherical biofilms (circled in red). The EDS analysis shows that the spheres are more carbon rich than the surrounding silicon rich substrate.